



HAL
open science

Structural and Magnetic Properties of Ferrofluids Composed of Self-Assembled Cobalt Ferrite Nanoflowers: A Multiscale Investigation

Malika Khelfallah, Claire Carvallo, Vincent Dupuis, Sophie Neveu, Dario Taverna, Yohan Guyodo, Jean-Michel Guigner, Enzo Bertuit, Laurent Michot, Walid Baaziz, et al.

► To cite this version:

Malika Khelfallah, Claire Carvallo, Vincent Dupuis, Sophie Neveu, Dario Taverna, et al.. Structural and Magnetic Properties of Ferrofluids Composed of Self-Assembled Cobalt Ferrite Nanoflowers: A Multiscale Investigation. *Journal of Physical Chemistry C*, 2024, 128 (31), pp.13162 - 13176. 10.1021/acs.jpcc.4c00790 . hal-04672318

HAL Id: hal-04672318

<https://hal.science/hal-04672318v1>

Submitted on 4 Nov 2024

HAL is a multi-disciplinary open access archive for the deposit and dissemination of scientific research documents, whether they are published or not. The documents may come from teaching and research institutions in France or abroad, or from public or private research centers.

L'archive ouverte pluridisciplinaire **HAL**, est destinée au dépôt et à la diffusion de documents scientifiques de niveau recherche, publiés ou non, émanant des établissements d'enseignement et de recherche français ou étrangers, des laboratoires publics ou privés.

Structural and Magnetic Properties of Ferrofluids Composed of Self-assembled Cobalt Ferrite Nanoflowers: a Multi-scale Investigation

Malika Khelfallah,¹ Claire Carvalho,¹ Vincent Dupuis,² Sophie Neveu,² Dario Taverna,¹ Yohan Guyodo,³ Jean-Michel Guigner,¹ Enzo Bertuit,^{1,2} Laurent Michot,² Walid Baaziz,⁴ Ovidiu Ersen,⁴ Ingrid Marie Andersen,⁵ Etienne Snoeck,⁵ Christophe Gatel,⁵ Amélie Juhin^{1}*

¹Sorbonne Université, Muséum National d'Histoire Naturelle, UMR CNRS 7590, IRD, Institut de Minéralogie, de Physique des Matériaux et de Cosmochimie, IMPMC, 75005 Paris, France

²Sorbonne Université, CNRS, Lab PHENIX, UMR 8234, F-75005 Paris, France

³Université Paris Cité, Institut de physique du globe de Paris, CNRS, F-75005 Paris, France

⁴IPCMS, UMR 7504, Université de Strasbourg, 23 rue du Loess, 67034 Strasbourg, France

⁵CEMES, CNRS UPR 8011, 29 Rue Jeanne Marvig, 31055 Toulouse, France

KEYWORDS: ferrofluid, magnetic nanoparticles, electron microscopy, magnetometry, FORC, magnetic dipolar interactions, magnetocrystalline anisotropy

ABSTRACT

Colloidal solutions of magnetic nanoparticles (ferrofluids) exhibit intriguing macroscopic properties that find their origin in the magnetic dipole interparticle interactions taking place at the nanoscale. Here we study experimentally the structuration and magnetic properties of a ferrofluid composed of 25 nm CoFe_2O_4 nanoflowers, which shows different types of nanoparticle assemblies with and without an external magnetic field. A combination of advanced magnetometry (First Order Reversal Curve measurements combined with simulations), transmission electron microscopy (high resolution and cryogenic transmission electron microscopy, electron tomography, electron holography) and small angle x-ray scattering techniques was used to build a comprehensive picture from the nano-scale to the macro-scale of this ferrofluid, from the collective behavior down to the particle level. Our results provide an original, extensive set of experimental quantitative data and make connection between the nanoscale organization and collective magnetic properties. Our findings also highlight the competition between magnetic anisotropy of CoFe_2O_4 nanoflowers and magnetic dipole interactions.

INTRODUCTION

Ferrofluids (FFs) are defined as colloidal suspensions of magnetic nanoparticles (MNPs) in a liquid. Nanoparticles have a typical diameter in the 5-25 nm range and are composed of a ferri/ferromagnetic material. Each MNP can be considered as a single magnetic domain, with a magnetic dipole moment on the order of $10^4 \mu_B$, where μ_B is the Bohr magneton ($9.24 \cdot 10^{-24}$ A.m²). FFs are considered as model systems for dipolar fluids. They find numerous current and potential applications in biomedicine (*e.g.*, magnetic hyperthermia,^{1,2} contrast agents for magnetic resonance imaging³), in technology (magnetic recording materials, sensor components)⁴ and art.⁵ These applications take advantage of their low cost and high chemical stability.⁶

The modification of macroscopic properties by an applied magnetic field finds its origin in the ferrofluid nanoscale structuration, where nanoparticles aggregate to form linear chain-like structures resulting from strong dipole-dipole interactions. Previous investigations have underlined the relevance of studying field-induced structures in ferrofluids, in order to optimize the efficiency of biomedical applications,⁷ to develop new magneto-optical applications⁸ or to understand original phase transitions occurring with temperature.⁹

At zero applied magnetic field, as initially predicted by De Gennes and Pincus,¹⁰ MNPs can self-assemble spontaneously when dipolar interactions in ferrofluids are large enough, *i.e.* the dipole-dipole energy exceeds thermal fluctuations, which is quantified by the ratio λ between the magnetostatic energy and the thermal energy. Theoretical simulations, such as Monte Carlo-based ones,^{11,12} have been used to calculate the structural assembly of particles as a function of λ , concentration, and temperature, and they have predicted the existence of nanoparticles self-assembled in chains, rings, or a combination of both. These assemblies significantly change the ferrofluid macroscopic properties.¹³⁻¹⁶

The Stoner-Wohlfarth model, commonly used to describe magnetic colloids with non-interacting, single domain MNPs with uniaxial anisotropy, does not account for dipole-dipole interactions. New models^{17,18} have been developed to include the influence of dipolar interactions in ferrofluids, allowing better refinement of FF magnetic properties, but these models have been so far mostly applied to spherical nanoparticles in a small size range (5-10 nm).

On the experimental side, chain-like assemblies have rarely been imaged directly, and only by cryo-transmission electron microscopy (cryo-TEM) in zero-field¹⁹ and field-cooled²⁰ experiments. Since these pioneering studies,¹⁹ information on clustering or aggregation of particles has been obtained experimentally by small-angle scattering measurements (with both X-rays and

neutrons),^{21,22} but they remain indirect probes and are not able to distinguish between the different shapes of assemblies predicted by simulations.¹¹ Other imaging techniques, such as electron holography²³ or magnetic force microscopy,²⁴ allow to make connection between nanoscale organization and local magnetic properties in assembled nanoparticles on dried samples, but few of these studies exist.^{25–29} In general, apart from bulk magnetometry experiments, experimental studies of FF remain scarce and there is especially a lack of quantitative investigation of particle assembly and its relationship with collective magnetic properties. A deeper understanding of this relationship would open new perspectives to design novel or more efficient magnetic responsive ferrofluids, by tuning magnetic dipolar interactions with magnetic anisotropy, size or shape of MNPs.

Most studies have so far focused on the influence of particle size, concentration and particle saturation magnetization on the formation of self-assembled structures at zero field. They have largely focused on magnetite Fe_3O_4 ,³⁰ maghemite $\gamma\text{-Fe}_2\text{O}_3$,³¹ iron,³² and more recently (but much less extensively) cobalt ferrite CoFe_2O_4 .³³ The effect of particle shape (cube, sphere, rod, flower...) has been little studied so far,³⁴ although it seems of strong potential interest. For example, it was shown that cubic particles in ferrofluids are more prone to form chains in zero magnetic field than spheres.⁷ Furthermore, flower-shaped multi-core nanoparticles (or nanoflowers) of magnetite have been shown to exhibit better hyperthermia performance than dense spherical nanoparticles with similar size,³⁵ but this was attributed to the multicore structure of nanoflowers rather than to particle assembly. The connection between the multi-core structure and their magnetic properties has attracted growing interest (see for example the recent study of Neumann et al.³⁶). Since the magnetic configuration of a nanoflower is difficult to reproduce with micromagnetic simulations,

being a disordered spin system with exchange interactions between the different cores, it is still presently unclear whether a nanoflower behaves like a single magnetic domain.

In this work, we studied experimentally a FF composed of cobalt ferrite nanoflowers in the 20 nm range dispersed in water. Our goals were to: (i) finely characterize the morphology and magnetic properties of these nanoflowers, (ii) elucidate the nature of the magnetic domain state (multidomain or single-domain), (iii) study in a quantitative way the assembling and magnetic properties under different interaction regimes and magnetic field (with or without) conditions. Chaining properties and colloidal stability were key factors in the choice of sample. Since cobalt ferrite is a hard magnetic material with an exceptionally high anisotropy constant, the nanoparticles can be considered as stable magnetic dipoles that do not exhibit time-dependent fluctuations about the easy axis of magnetization. In addition to conventional techniques (X-ray Diffraction XRD, bulk magnetometry, standard TEM), advanced experimental approaches were combined to access (i) the single particle morphology and crystal structure (high resolution TEM, electron tomography), (ii) the quantitative nanoscale characterization of particles assemblies (cryo-TEM, preserving the native organization in the FF), (iii) the collective macroscopic assembling properties (SAXS), (iv) the distribution of magnetic coercivity and interaction fields (measurement and simulation of First Order Reversal Curve FORC diagrams), (v) the local orientation of magnetic moments within particle assemblies (electron holography). Using this methodology, we were able to build a comprehensive multi-scale picture of this FF, from the collective behavior down to the particle level, and we provide a set of original quantitative findings on its self-organization and magnetic properties.

METHODS

Synthesis

Cobalt ferrite nanoflowers were obtained by using the polyol process³⁷ which consists in a forced hydrolysis of Fe^{3+} and Co^{2+} mixture in a polyol solution. Depending on the polyol used for the synthesis, the obtained nanoparticle morphology differs. When the reaction is realized in a mixture of diethylene glycol (DEG) and N-methyl diethylamine (NMDEA) (50:50 V:V), nanoflower-shaped nanoparticles are obtained.³⁸ In order to obtain a stable colloidal suspension at pH7, the surface of the MNP is functionalized by citrate molecules.³⁹ CoFe_2O_4 is a cubic spinel oxide with $Fd\bar{3}m$ space group symmetry, where cobalt (Co^{2+}) and iron (Fe^{3+}) cations are distributed between tetrahedral and octahedral sites.

Chemicals:

N-methyldiethanolamine (NMDEA, >99%), diethylene glycol (DEG, >99%), iron(III) chloride hexahydrate ($\text{FeCl}_3 \cdot 6\text{H}_2\text{O}$, 99%), iron(II) chloride tetrahydrate ($\text{FeCl}_2 \cdot 4\text{H}_2\text{O}$, 99%), cobalt(II) chloride hexahydrate ($\text{CoCl}_2 \cdot 6\text{H}_2\text{O}$, 99%) and manganese(II) chloride tetrahydrate ($\text{MnCl}_2 \cdot 4\text{H}_2\text{O}$, 99%) were purchased from Merck (Darmstadt, Germany). Sodium hydroxide pellets (NaOH, 99%), hydrochloric acid (HCl, 37%), ethanol (96%), nitric acid (HNO_3 , 68%), acetone (>99%), and diethyl ether (Et_2O , 100%) were purchased from VWR International (Rosny-sous-Bois, France). All chemicals were used without further purification.

Protocol:

$\text{FeCl}_3 \cdot 6\text{H}_2\text{O}$ and $\text{CoCl}_2 \cdot 6\text{H}_2\text{O}$ were dissolved in a mixture of DEG (40 mL) and NMDEA (40 mL). At the same time, NaOH pellets were grinded and dissolved overnight in a mixture of DEG (20

mL) and NMDEA (20 mL). The two solutions were mixed by magnetic stirring for 1 h and then heated at 200°C during 4 hours.

Experimental methods

a. Crystal structure determination by X-Ray Diffraction (XRD)

The crystalline structure and coherent domain size of the nanoparticles were determined with a PANALYTICAL X'pert Pro MPD diffractometer with the CoK α radiation ($K\alpha = 1.79 \text{ \AA}$) at IMPMC (Paris, France). All diffraction peaks can be indexed with the CoFe₂O₄ spinel structure (reference code pattern 96–5941-0064). From the XRD profile of the (311) peak, the nanospinel size (d_{XRD}) was computed with the Debye-Scherrer expression.⁴⁰

b. Chemical titration

The cationic concentrations of cobalt and iron were determined by Atomic Absorption Spectrometry after dissolution of the nanoparticles in concentrated hydrochloric acid. We used a Perkin Elmer Analyst 100 spectrometer with an air-acetylene flame at a mean temperature of 2300°C (PHENIX laboratory, Paris, France). Experiments were repeated three times. The cobalt molar ratio X_m is defined as follow:

$$X_m = \frac{[Co]}{[Co] + [Fe]}$$

c. Thermogravimetric Analysis

The corresponding mass of organic matter in the functionalized MNP was measured by Thermogravimetric Analysis (TGA) and subtracted in order to obtain the proper mass of magnetic material, using a TA-TGA550 Discovery series operating in high-resolution mode with a heating speed of 20°C/min in the range 20°C–600°C.

d. Small Angle X-ray Scattering

Small Angle X-ray Scattering (SAXS) gives information on the structural properties of the sample, both on the individual nanoparticle (shape, surface, size) and the collective behavior. SAXS experiments were carried out at PHENIX laboratory (Paris, France) on a Xeuss 2.0 equipment equipped with a GeniX source operating at $\lambda = 1.54 \text{ \AA}$ and a Pilatus detector. Samples were conditioned in glass capillaries with a diameter of 1mm, and two sample-to-detector distances, 0.3 m and 2.5 m. In such conditions, the investigated q -range (where $q=4\pi\sin(\theta)/\lambda$ where θ is half of the diffusion angle) ranges from $\approx 4 \cdot 10^{-3}$ to 1.2 \AA^{-1} . For experiments involving a magnetic field, a magnet was placed near the sample with the magnetic field ($\approx 300 \text{ mT}$) oriented parallel to the capillary, and the SAXS pattern was then recorded.

e. Transmission Electron Microscopy

Different Transmission Electron Microscopy (TEM) observations were carried out in order to characterize the nanoflowers and their organization within the different samples. Standard TEM was used to obtain the statistical distribution of particle sizes in each sample. High Resolution TEM (HR-TEM) provided an insight on the crystalline structure within individual nanoflowers. Both Standard TEM and HRTEM observations were realized with a JEM2100F (JEOL, Japan) microscope equipped with a Schotky FEG gun, operating at 200 kV.

In addition, cryo-TEM was used to preserve the spontaneous organization of nanoparticles, since it does not require drying the sample on a TEM grid. Cryo-TEM samples grids were prepared in a automatic cryo-plunger (LEICA, Germany). A 5 μL drop of the initial sample solution was deposited on “quantifoil”[®] (Quantifoil Micro Tools GmbH, Germany) carbon membrane grids previously plasma cleaned for 30s on the membrane side. The excess of liquid on the grid was absorbed with a 3s blotting with a filter paper, and the grid was frozen quickly in liquid ethane to form a thin vitreous ice film. Once placed in a cryo-holder (GATAN, USA) cooled with liquid nitrogen, the samples were transferred to the microscope and observed at low temperature (-180 °C). Cryo-TEM images were recorded on ultrascan 1000, 2k x 2k pixels CCD camera (Gatan, USA), using a JEM2100 (JEOL, Japan) microscope equipped with a LaB₆ electron gun operating at 200 kV.

f. Electron tomography

Electron tomography allows a three-dimensional observation of the nanoflowers by imaging the sample at different angles. Electron tomography experiments were realized at IPCMS (Strasbourg, France) using a JEOL 2100 FEG S/TEM microscope operated at 200 kV equipped with a spherical aberration corrector on the probe-forming lens. Samples were dispersed by ultrasonication in ethanol and deposited on a holey carbon coated TEM grids. The acquisition of tilt series was acquired in TEM mode using the tomography plug-in of the Digital Micrograph software by tilting the specimen in the angular range +67.5 and -70.5 using an increment of 1.5° in the equal mode, giving thus a total number of images equal to 93 images.

The recorded images of the tilt series were spatially aligned by cross-correlating consecutive images using IMOD software. For the volume calculation, we have used the algebraic

reconstruction technique (ART) implemented in the TomoJ plugin working in the ImageJ software were thus used to compute the reconstructed volumes. Finally, the visualization and the analysis of the final volumes were carried out using the displaying capabilities and the isosurface rendering method in the Slicer software.

g. Electron holography

Electron holography allows to image the magnetic induction lines produced by the nanoparticles inside an assembly previously observed by cryo-TEM. Electron holography experiments²³ were carried out at CEMES (Toulouse, France). A lacey, carbon coated TEM grid was plasma cleaned for 20 s and a 5 μL drop of the ferrofluid was deposited on the grid. The measurements were carried out at room temperature. First, we located MNP assemblies similar to the ones previously observed by cryo-TEM. We then measured the hologram of the assembly by making the transmitted electron beam interfere with a reference beam going through a hole in the grid. The same hologram was measured again after turning the grid by 180° in order to remove the phase shift contribution from the electric potential of the nanoparticles. It was ensured that no stray field altered the magnetic configuration during the experiment through the use of a Lorentz stage set-up. The resulting image after treatment shows the magnetic induction lines projected in the plane of the grid.

h. Magnetometry

Hysteresis loops were measured with a Magnetic Properties Measurement System (MPMS-XL) on a frozen liquid sample from -2 T to 2 T with a 50 mT step size, on a drop of 20 μL in an

Eppendorf. Saturation magnetization was also measured on a weighted powder (~10 mg in a gel cap) at room temperature.

First-Order Reversal Curve (FORC) diagrams allow a qualitative characterization of the magnetic domain structure and magnetostatic interactions, by measuring a set of partial hysteresis curves that originate from the descending branch of the hysteresis loop^{41,42} FORC diagrams were measured at the IPGP-IMPIC Mineral Magnetism Analytical Facility (Paris, France) with a magnetometer (μ -VSM) from Princeton Measurements Corporation equipped with a cryostat. For stable single domain particles, in first approximation, the FORC distribution along the vertical axis can be interpreted as the distribution of the interaction field of particles, and the marginal FORC distribution as the coercivity distribution of the system.^{41,43} The marginal distribution is obtained by integrating the signal along the vertical axis⁴⁴ while the vertical distribution is a vertical profile of the FORC diagram measured at the maximum of the marginal distribution.

FORC diagrams were each constructed from 134 individual FORCs measured with a field step of 15 mT, at a temperature of 100 K, and with an averaging time of 0.3 s. The measurement time for each FORC diagram was about one hour. They were subsequently analyzed with the FORCinel software,⁴⁵ with a variable smoothing factor.⁴⁶ The variable smoothing considerably reduces the noise levels by applying larger smoothing factors to the background, while preserving the areas along the axes with relatively small smoothing factors.

Three FORC diagrams were measured on each sample. First, 20 μ L of the liquid ferrofluid was enclosed in a polycarbonate gelcap and centered between the coils. The sample was cooled in zero-field to 100 K, and a first FORC diagram was measured (ZFC measurement). Then, the sample was reheated to room temperature, cooled in a field of 1.8 T, and a second FORC diagram was

measured (FC measurement). Finally, the VSM head to which the sample is attached was turned by 90° , and a third FORC diagram was measured (FC90 measurement).

The FORC diagrams were plotted using the FORCinel⁴⁵ software with a VARIFORC⁴⁶ smoothing parameters $\{S_{c,0}, S_{c,1}, S_{b,0}, S_{b,1}, \lambda_c, \lambda_b\} = \{7, 10, 7, 10, 0, 0\}$ defined in Ref. 44. In other words, the smoothing factor along the vertical and horizontal ridges is 7 and it is 10 elsewhere.

Simulation of FORC diagrams

In order to improve the qualitative analysis of FORC diagrams, we carried out simulations using the FORCulator software.⁴⁷ The FORCulator algorithm solves the Landau-Lifshitz-Gilbert equations with a damping factor $\alpha = 0.9$, for a specific configuration of N monodisperse nanoparticles with diameter d in a box of $500 \times 500 \times 500$ nm and saturation magnetization $M_s = 480$ kA/m. The nanoparticles can be either randomly distributed in space or form chains. Each specific chain configuration depends on the following parameters: the number of chains (N_{chain}), the number of particles per chain (N_{NP}), the distance between particles in a chain e , the rigidity of the chain or collapse factor (c , $0 \leq c \leq 1$ with $c = 0$ for a perfectly straight chain) and the general orientation of the chains along the axis x , y , z of the simulation box, ($[x \ y \ z]$). The applied field during the calculation is oriented along the z axis. Polydispersity is taken into account in the model by introducing a lognormal distribution of anisotropy or switching fields with mean β and polydispersity σ . The values chosen here are $\sigma = 0.3$ and $\beta = 2$, which corresponds to a maximum centered at 120 kJ/m³. They were determined by fitting the experimental FORC marginal distribution of the sample measured in ZFC configuration with a lognormal function. The anisotropy easy axis can be randomly distributed in space or aligned with the axis of the chains.

For each configuration, 200 individual FORCs were calculated with a field step of 10 mT and coercivity (B_c) ranging from 0 to 1000 mT and interaction field (B_u) ranging from -100 to 100 mT. In order to increase the quality of the data, N_{avg} configurations were averaged together to obtain the final FORC diagram. The total number of particles simulated ($N_{NP} * N_{chain} * N_{avg}$) is always equal to 5000 at minimum to ensure good statistics. One simulation typically lasted from 15 to 20 hours.

Based on our cryo-TEM observations, a ZFC configuration was modeled by considering $N_{chains} = 5$ chains of $N_{NP} = 10$ nanoparticles each, separated by $e = 2$ nm. The chains are randomly oriented in space ($[x y z] = [0 0 0]$) and the rigidity $c = 0.6$ to simulate the mix between chains, rings and networks observed in cryo-TEM images. A total of $N_{avg} = 100$ configurations were simulated.

In the FC configuration, the chain length was increased to $N_{NP} = 50$ particles with the interparticle distance kept to $e = 2$ nm also. The number of chains $N_{chain} = 5$ is not large enough to introduce interactions between the chains. The collapse factor was reduced to $c = 0.02$ to obtain almost parallel chains, all oriented along the direction of the applied field ($[x y z] = [0 0 1]$). A total of $N_{avg} = 20$ configurations was simulated.

For the FC90 configuration, we used the same parameters as in the FC configuration but the chains are oriented in a direction perpendicular to that of the applied field ($[x y z] = [1 0 0]$).

The FORCulator software was originally built to simulate FORC diagrams of magnetite at room temperature, therefore our simulations are set at 300 K and the saturation magnetization is set to that of magnetite. However, it is possible to fix the value of individual moments $\mu = VM_s$ to that of CoFe_2O_4 by artificially modifying the size of individual particles.

Individual particles of cobalt ferrites have a cubic anisotropy, however the organization in chains that is observed experimentally causes the effective anisotropy to be uniaxial. Therefore, we chose to run our simulations with uniaxial anisotropy particles, as is also often done in other micromagnetic simulations (e.g., Usov *et al.*¹³). The number of particles per chain in the ZFC configuration $N_{NP} = 10$ was chosen as a compromise between the mean number of particles per chain $N_{NP} = 5$ and per ring $N_{NP} = 12$ found in cryo-TEM images (Fig. 5).

Despite all these limitations, the simulations of FORC diagrams are nonetheless useful as a first approach for a qualitative study of the variations in FORC diagrams depending on the configuration.

The VARIFORC⁴⁶ smoothing parameters used to plot the FORC diagrams are 5 along the horizontal and vertical ridges and 8 elsewhere (in other terms, $\{S_{c,0}, S_{c,1}, S_{b,0}, S_{b,1}, \lambda_c, \lambda_b\} = \{5, 8, 5, 8, 0, 0\}$ as defined in the VARIFORC protocol).

RESULTS/DISCUSSION

Characterization of single nanoflowers.

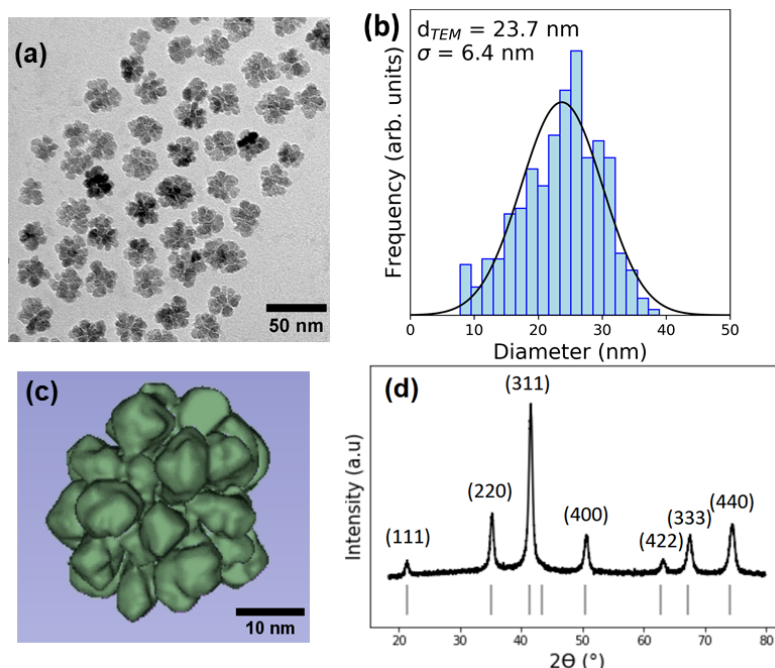


Figure 1. (a) TEM image of the CoFe_2O_4 nanoflowers synthesized by polyol process³⁷. (b) Diameter distribution fitted by a lognormal function. (c) Example of 3D reconstruction of a nanoflower obtained by electron tomography. (d) XRD pattern measured on a dried FF sample with indexed diffraction peaks corresponding to the spinel phase of CoFe_2O_4 .

From TEM images (Fig. 1a), the nanoparticles exhibit well-defined multi-core structures with a mean diameter $d_{TEM} = 23.5$ nm and a standard deviation $\sigma = 6.4$ nm (Fig. 1b). Nanoflowers are defined as densely packed aggregates forming a flower-shaped nanosized particle. XRD patterns (Fig. 1d) measured on a dried FF sample confirm the presence of a spinel phase with a lattice parameter $a \approx 8.37$ Å and a coherent size d_{XRD} of 13 nm, which is smaller than the size determined by TEM (Tab. S1). The cobalt molar ratio $X_m = 20\%$ measured by chemical titration shows that the nanoflowers are under-stoichiometric and can be formulated as $\text{Co}_{0.6}\text{Fe}_{2.4}\text{O}_4$. This molar ratio is lower than other cobalt ferrite synthesis (Daffé *et al.*⁴⁸ with $26.4\% < X_m < 35.5\%$ or Torres *et al.*⁴⁹ with $18.2\% < X_m < 30.3\%$). In these studies, it was found that molar ratio and particle size alone cannot determine magnetic properties such as coercivity and remanence. Measurements sensitive to cation occupancy are needed (see Ref. 50).

Electron tomography measurements performed on single nanoflowers (Fig. 1c) show that the nanoparticles are formed by smaller (~ 7 nm) crystallites (or “petals”) aggregated around a core. Three-dimensional reconstruction also evidences the presence of small cavities (~ 3 nm) inside some petals (Fig. S1). A total of four particles was observed by tomography with an average diameter (as measured from 2D images) of $31.2 \text{ nm} \pm 0.2 \text{ nm}$, thus larger than d_{TEM} . The analysis of the tomography images yields an average total volume of $10300 \pm 1080 \text{ nm}^3$. This value is 35 % smaller than the volume of a sphere with similar diameter. Moreover, surface was estimated to $4510 \pm 363 \text{ nm}^2$, which is 45 % higher than the surface of a perfect sphere with similar diameter. Finally, the specific surface was calculated to $83 \text{ m}^2/\text{g}$. As a comparison, Lartigue *et al.*⁵⁰ found using nitrogen adsorption measurements a specific surface of $82 \text{ m}^2/\text{g}$ for iron oxide flowers 29 nm in diameter, which is consistent with our findings.

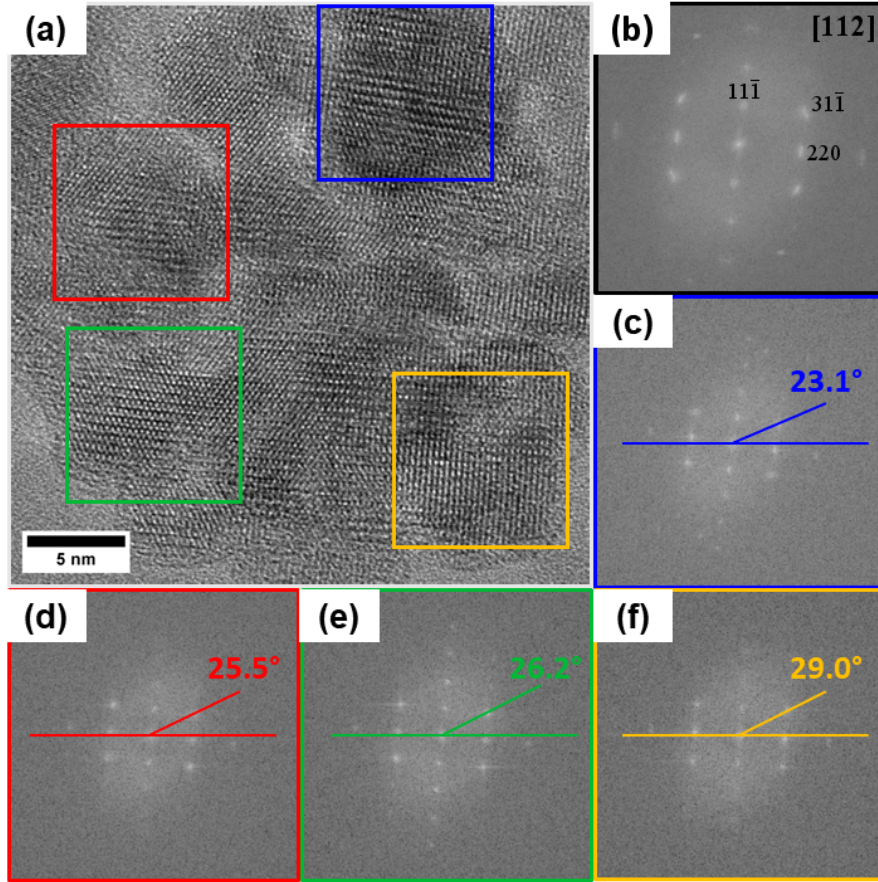


Figure 2. (a) HRTEM image of a nanoflower, (b) Fast Fourier Transform (FFT) of the whole image, (c)-(f) FFT of different areas in the particle with the angle measured between the same hkl diffraction peak and the reference horizontal axis.

At the nanoscale, nanoparticles present a complex crystalline structure. Due to the chemical process during synthesis, small crystallites start to form before agglomerating in larger nanoparticles⁵¹. Using HRTEM, the particle structure can be resolved (Fig. 2a). The Fast Fourier Transform (FFT) of the HR image (Fig. 2b) highlights diffused spots, caused by the so-called “mosaicity” within a single nanoparticle⁵². Fig.2c-f shows the FFT patterns measured from different areas of a typical nanoparticle. A spot corresponding to a specific hkl plane family (here 311) was arbitrarily chosen, and the angle between this node and a reference horizontal axis was measured, see Fig. 2. The angular spread is of the order of 6° for this specific nanoparticle. Similar

deviation angles were found for all the nanoparticles measured by HRTEM. The nanoflowers are thus composed of crystallites arranged in a similar crystalline orientation but slightly tilted from one crystallite to another. This result is consistent with previous HRTEM nanoflowers observations,^{50,52–54} although the angular spread between the crystallites was found to be smaller in those studies (between 1° and 3°). The mosaicity of the nanoparticles can explain the smaller sizes found by XRD ($d_{XRD} < d_{TEM}$), since diffraction is sensitive to the crystallites and not the whole nanoflowers.

Evidence of particle assemblies from SAXS.

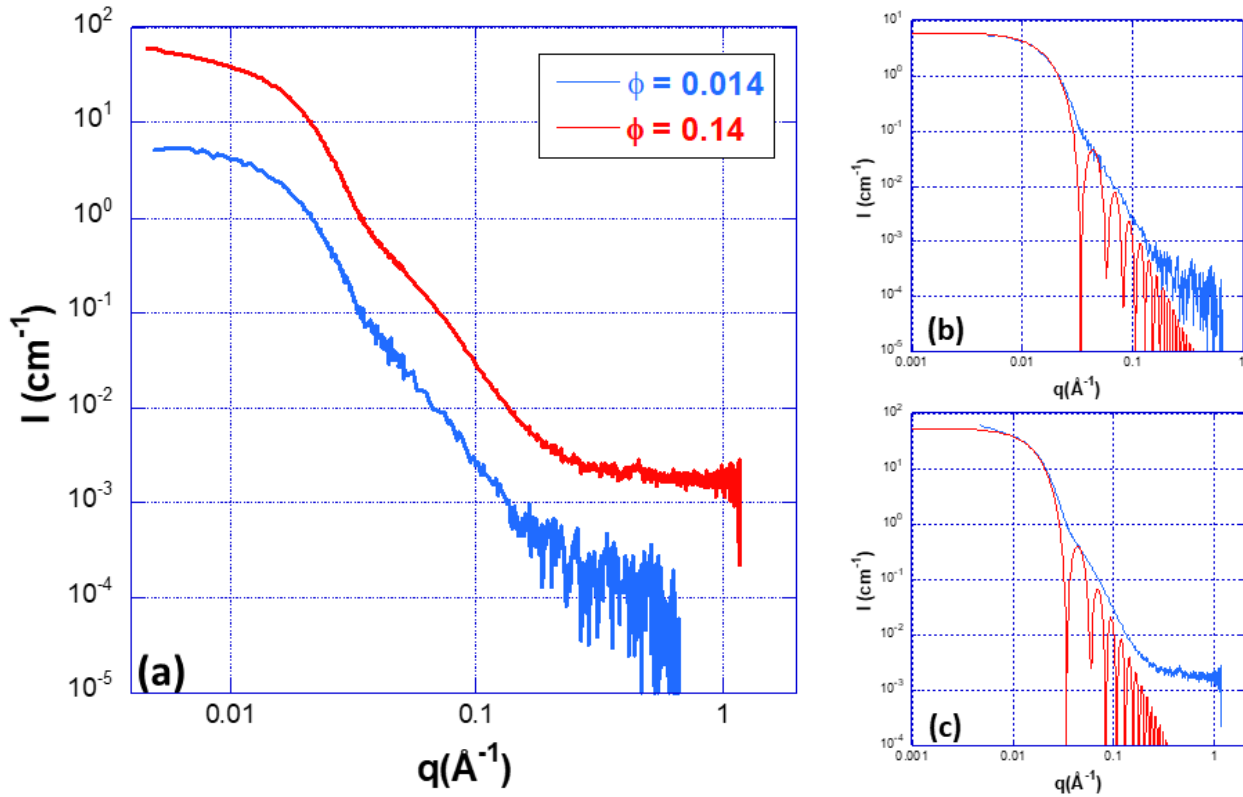


Figure 3. Radial distribution of the SAXS pattern measured for two volume fractions, (a) $\phi = 0.014\%$ (blue curve) and $\phi = 0.14\%$ (red curve). Comparison between the experimental curve and the calculated form factor of monodisperse spheres for volume fractions (b) $\phi = 0.014\%$ and (c) $\phi = 0.14\%$.

Figure 3a presents the SAXS curves measured in the absence of any magnetic field for samples with volume fractions $\phi = V_{NP} / V_{total}$ of 0.014 % and 0.14 %. Both curves display a similar shape with variations in intensity that are in line with the differences in volume fraction. Both curves were compared with the SAXS curves corresponding to the form factor of monodisperse spheres (Figs. 3b, c and S2). Several results can be deduced from this comparison : (i) both curves are well approximated by a form factor corresponding to a sphere⁵⁵ with a diameter of ~ 26 nm; (ii) the absence of marked oscillations in the experimental curves reveals that the particles are polydisperse, a conclusion in line with TEM results presented hereafter; (iii) the deviation at high q of the slope of the SAXS curve from the q^{-4} dependence (exhibited by the envelope of the spherical form factor) suggests that the surface of the particles displays significant roughness;⁵⁶ (iv) at low q the behavior of both systems is different: the particles at a volume fraction of 0.014% display a plateau that follows the form factor of spheres (Fig. 3b), whereas for a volume fraction of 0.14% (Fig. 3c) an upward deviation is observed. This reveals the presence of larger objects corresponding to associated particles in the suspension. The low slope observed in this region might be tentatively assigned to the presence of chains of particles. However, the q range on which this is observed is too limited to provide a definitive interpretation.

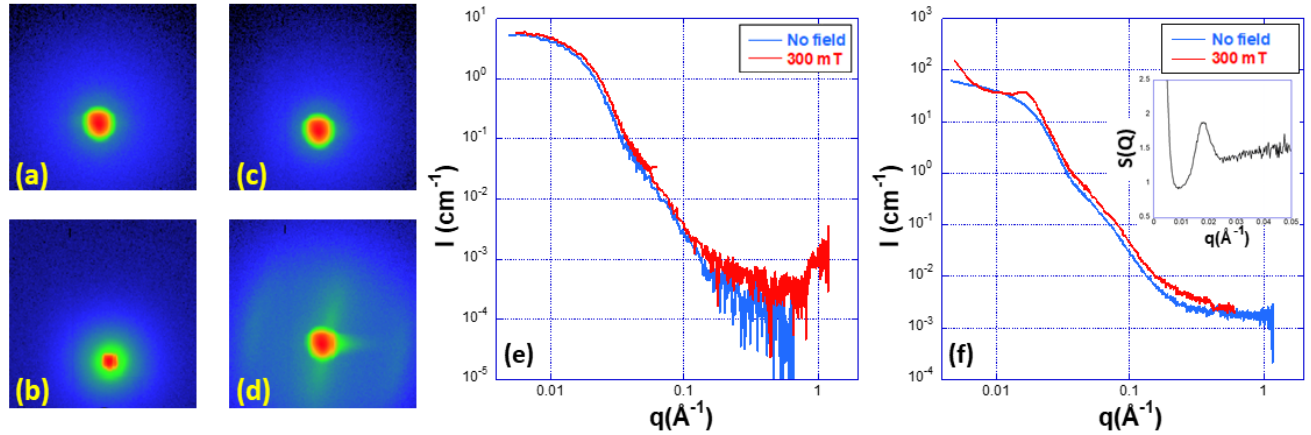


Figure 4. Bidimensional scattering patterns for (a) $\phi = 0.014\%$ without magnetic field and (b) $\phi = 0.014\%$ with magnetic field, (c) $\phi = 0.14\%$ without magnetic field and (d) $\phi = 0.14\%$ with magnetic field. Radial distribution for volume fractions (e) $\phi = 0.014\%$ and (f) $\phi = 0.14\%$ (inset represents the structure factor obtained from the intensity of the curve with field divided by the intensity of the curve without field).

Figure 4 shows the influence of a magnetic field (≈ 300 mT) on the SAXS patterns of suspensions with volume fractions of 0.014 % and 0.14 %. Figures 4a and 4b present the bidimensional scattering pattern obtained for the sample with a volume fraction of 0.014% in the absence and presence of a magnetic field, respectively. No significant differences are observed, which shows that for this sample, at the scale probed by SAXS, no visible structure appears under a magnetic field. This is confirmed by the integrated data (Fig. 4e) that do not exhibit any significant differences related to the application of a field. The situation is markedly different in the case of the sample with a volume fraction of 0.14%. Indeed, when compared to the bidimensional scattering pattern in the absence of a magnetic field (Fig. 4c), the pattern obtained with a magnetic field (Fig. 4d) clearly exhibits anisotropic features that can be assigned to the presence of almost vertically oriented objects. This can also be noticed by looking at the integrated signal (Fig. 4f). Under an applied magnetic field, a structure factor appears with a peak located at $\approx 0.0182 \text{ \AA}^{-1}$ (inset of Fig. 4f). This corresponds to a distance of ≈ 34 nm. Considering that the MNPs have a

diameter of 26 nm (as determined by SAXS, which is more sensible to large objects than small ones), this reveals the presence in the system of particle aggregates that are not in close contact but are separated by less than 8 nm. This is in agreement with the cryo-TEM investigations featured in the next part (Fig. 5c). Furthermore, data at low q display an upward deviation that can be assigned to the existence of larger structures, such as chains. At low q , an evolution in q^{-1} would be expected for isolated chains. However, this slope is not observed here, which suggests the presence of dense stacks or branched networks.

Imaging of MNP assemblies by cryo-TEM.

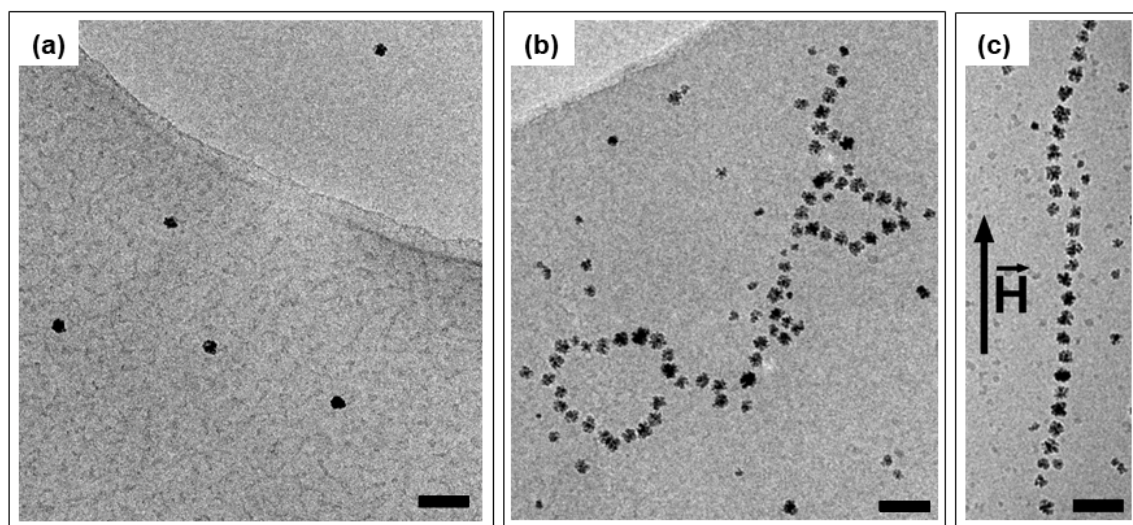


Figure 5. Representative cryo-TEM images for (a) $\phi = 0.014\%$, (b) $\phi = 0.14\%$ and (c) $\phi = 0.14\%$ with an external magnetic field H applied before freezing (scale bar = 100 nm).

In order to image particle assemblies, cryo-TEM observations were performed on a dilute ($\phi = 0.014\%$) and a concentrated ($\phi = 0.14\%$) FFs. While the former shows isolated, non-interacting nanoparticles (Fig. 5a), self-assembly is observed in the latter, with nanoparticles

forming small chains, rings and branches (Fig. 5b). Finally, under a 25mT magnetic field, nanoparticles form long micrometric chains aligned along the field direction (Fig. 5c).

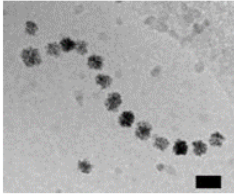

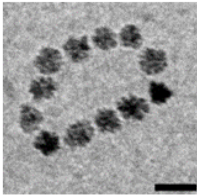
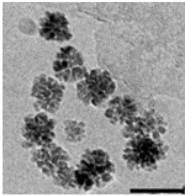
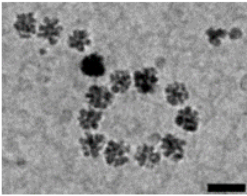
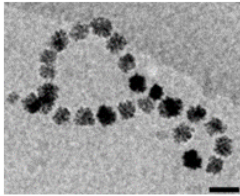
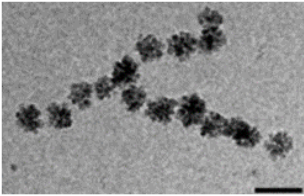
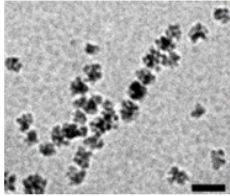
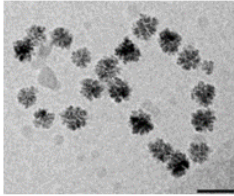
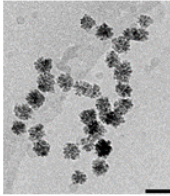
Types of self-assembly				Total
 Chain: 51%				Chains 62%
 Chain with defect: 11%				
 Ring: 7%	 Ring with defect: 5%	 Ring and chain: 6%	 Double ring: 2%	Rings 20%
 Y-shape: 4%	 X-shape: 1%	 Ring with double chain: 1%	 Branches: 12%	Networks 18%

Figure 6. Statistical analysis on cryo-TEM images with the associated percentage of occurrence for concentration $\phi = 0.14\%$ without field (scale bar = 50nm).

Furthermore, we analyzed 453 images containing assemblies, and calculated the statistical probability of appearance of a certain assembly amongst the ones observed (note that this is different from the probability of observing the corresponding self-assembly, since isolated particles were not included in the counting). The sorted assemblies are mostly a combination of small chains and rings (Fig. 6). We established a classification based on that of Kantorovich *et*

*al.*¹¹ The statistical analysis shows that chains are the most probable assembly to form with a 62% probability. Small rings mixed with chains or other rings have a 20% probability while intertwined chains forming networks appear in 18% of the cases. A closer look at each category shows that well-defined, isolated chains are very frequent (51%). Other types of assemblies were less likely to appear, such as the double crossing chain or “X-shape” assembly at only 1% (or 5 cases), and the double ring at 2% (8 cases). The remaining 12%, a branched mix of chains and rings, do not fit into previous categories and are labeled “branches”.

Kantorovich *et al.*¹¹ used Monte-Carlo simulations to estimate, at similar particle concentration and temperature, that the assemblies were composed of 73% of chains and 23% of rings, with ~4% of other shapes. These values are consistent with our findings.

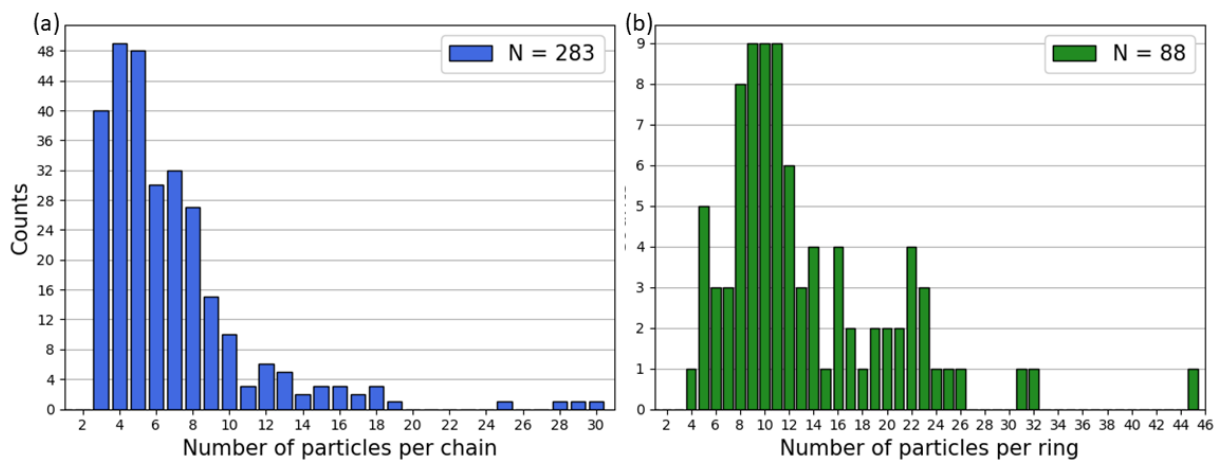


Figure 7. Distribution of the number of particles per (a) chain and (b) ring for cryo-TEM images. N is the total number of chains or rings.

The number of particles per assembly was also counted for chains and rings (Fig. 7). Although it varies substantially, the most probable particle number for a chain is 4 and 11 for a ring. The average number of particles per chain is globally lower for chains than for rings, which is in line

with the fact that when the chain length increases, it becomes energetically favorable to turn into a ring. Moreover, a distance of 4.7 ± 3.3 nm between nanoparticles was measured in assemblies of chains and rings.

Imaging of local magnetic configurations within MNP assemblies.

Electron holography was employed to image the local magnetic configuration of assemblies of nanoparticles. By comparison to previous holography studies performed on nanoparticles,^{24,27,28,57} it shall be noted that the low remanence of cobalt ferrite at room temperature introduces an additional complexity to the measurements.

Fifteen different assemblies were measured (Fig. S3) with five typical examples presented in Fig. 8. Phase images of the mean inner potential are shown in the left column. We added isophase contours calculated from the magnetic contribution to the electron phase shift: induction lines are parallel to these isophase contours. On the right are presented amplitude images extracted from the same holograms. The orientation of the in-plane projected magnetization for each particle is represented by red arrows. Fig. 8a-b show a ring-shaped assembly, with closed, rotating magnetic induction lines. In this case the magnetic moments are aligned head-to-tails, as would be the case for a system dominated by dipolar magnetic interactions to minimize the magnetic dipolar energy. Similarly, Fig. 8c, d shows a chain assembly with most moments aligned head-to-tail, except for one MNP in the center of the chain presenting an out-of-plane magnetization, represented by a circle. The out-of-plane particle is situated next to a smaller particle which could act as a defect in the magnetic chain. Anti-parallel coupling between two interacting chains is also observed (Fig. 8e, h) in agreement with previous study²⁷ where particles are next to each other in such configuration. In addition, antiparallel alignment of particles can also be obtained within a chain

with a projected magnetization perpendicular to the axis of the chain or perpendicular to the plan of the substrate (Fig. 8i, j).

While dipolar magnetic interactions dominate the organization of particles in rings, it seems that individual magnetocrystalline anisotropy must be taken into account when particles are arranged in chains, as evidenced by the fact that not all particle moments are aligned head-to-tail in this configuration.

It is worth to notice that the preparation method for electron holography observations necessitates the deposition of a drop on a TEM grid, and that the subsequent solvent evaporation can alter the orientation of the nanoparticles (and therefore their magnetic moment). However, as the particle assemblies are very similar to the ones observed by cryo-TEM, we can assume that the measured magnetic configurations are also closely related to native configurations in the liquid phase.

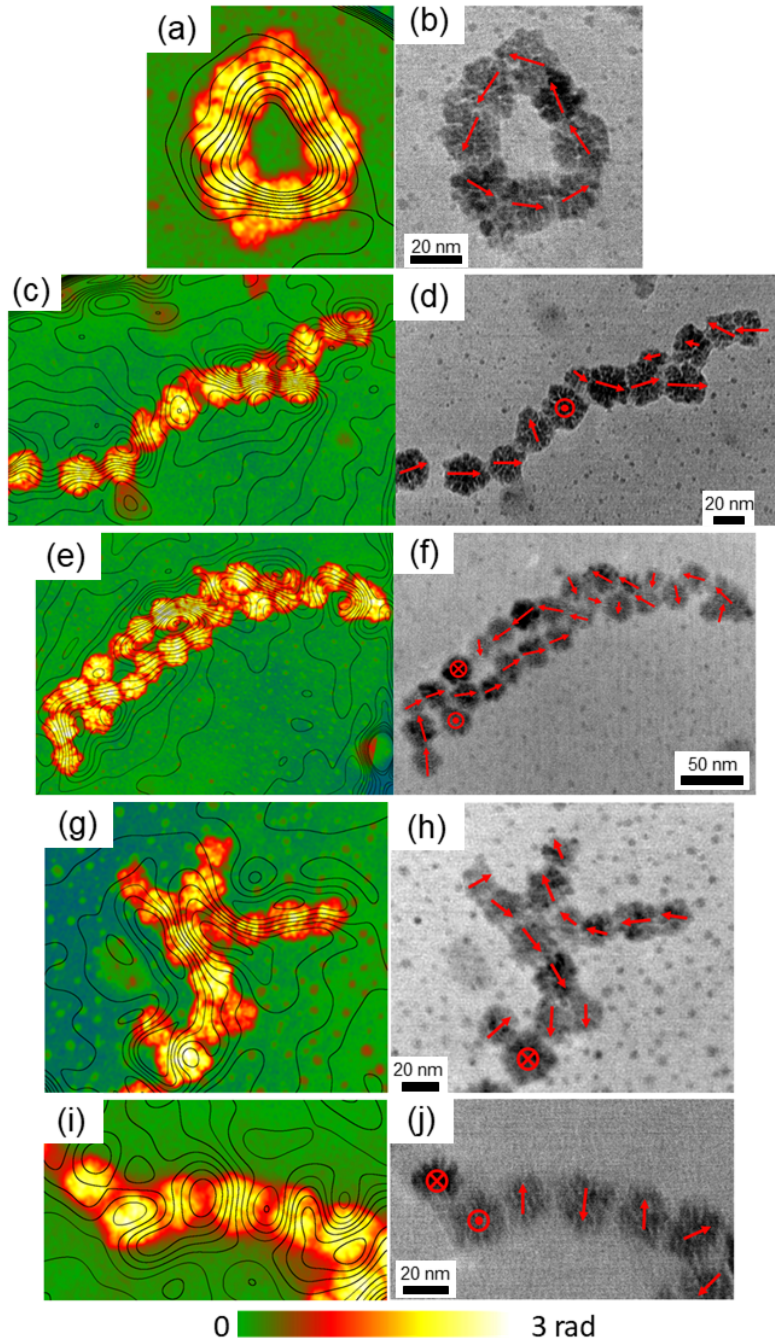


Figure 8. Phase and amplitude images obtained by electron holography on a sample prepared in zero field. (a, c, e, g, i) phase images of the mean inner potential (MIP) for different assemblies with magnetic induction lines extracted from magnetic phase images with 2 mrad isophase contours, (b, d, f, h, j) amplitude images with scale bar extracted from the same holograms than the phase images with added direction of the projected magnetization on each particle (red arrows).

Collective magnetic properties from magnetization curves.

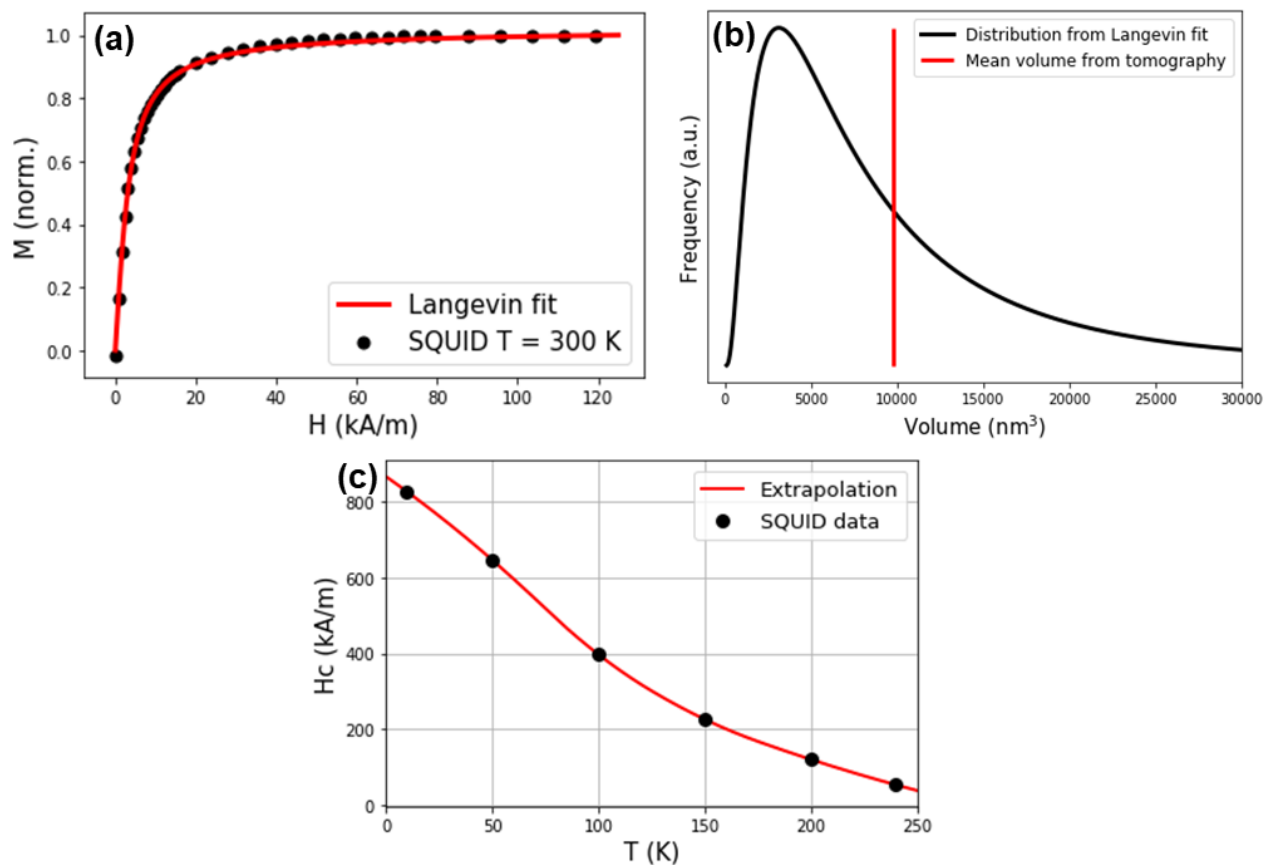


Figure 9. (a) Magnetization curve (black dots) measured by SQUID on a dilute sample at 300K and its volume-weighted Langevin fit (red line) (b) Resulting magnetic volume distribution (black line) compared to the mean volume measured in electron tomography (red line). (c) Variation of coercivity as a function of temperature (data points in black, extrapolation in red).

The saturation magnetization (M_s) measured at $T=300$ K on a powder (i.e., a dried sample of FF) yields a value corrected by Thermogravimetric Analysis (TGA) of 264 kA/m. This value is close to the value measured by Fu *et al.*⁵⁸ of $M_s = 234$ kA/m for cobalt ferrite nanoflowers (168 nm in diameter) but lower than the bulk saturation magnetization expected to 425 kA/m.⁵⁹ To explain this discrepancy, the magnetization curve measured on the dilute FF sample at 300 K was fitted by the Langevin model weighted by a lognormal distribution of the volumes (Fig. 9a). The resulting magnetic volume distribution (Fig. 9b) gives $V_0 = 7194$ nm³ and $\sigma = 0.9$. The average

volumes extracted from the electron tomography measurements correspond to the higher side of the distribution, showing that some amount of disordered spins does not contribute to the magnetic moment of the particle. Indeed, if we consider a layer of thickness $d = 0.6$ nm and the surface measured in tomography $S = 4510$ nm², one obtains a volume of disordered spins $V_{disorder} = d \cdot S = 2706$ nm³. From the study of Bishop *et al.*,⁶⁰ the saturation magnetization decreases to $M_s = M_s^{bulk} [(V_{total} - V_{disorder})/V_{total}]$. Considering $V_{disorder}$, we find that the saturation magnetization is reduced to $M_s = 313$ kA/m, which is closer to the present experimental value. Thus, the morphology of the nanoflowers and their high surface to volume ratio can partially explain the reduction in M_s .

Temperature-dependent magnetization curves show a magnetically blocked state below the fusion temperature of the solvent. The coercive field B_c was measured between 10 and 250 K and reaches 1 T at 10 K, a large value that is in line with other studies performed on cobalt ferrite nanocubes⁶¹ and nanospheres⁶² with similar Co/Fe molar ratio ($B_c \sim 1.2$ T and 2 T respectively). By extrapolating the coercive field vs temperature curve (Fig. 9c) to $T \rightarrow 0$ K, a value for the effective anisotropy constant K_{eff} was determined to 250 kJ/m³ using the Stoner-Wohlfarth model⁶³: $B_c \approx K_{eff}/M_s \mu_0$. The coercivity B_c was extracted from magnetization curves measured on a dilute FF, to prevent magnetic interactions between the nanoparticles. The nanoflowers exhibit a large magnetic anisotropy that strongly contributes to the magnetic properties of the FF. In other ferrites, the magnetocrystalline anisotropy is lower by more than one order of magnitude ($\sim 1-10$ kJ/m³)⁵⁹.

Distribution of magnetic properties from FORC diagrams.

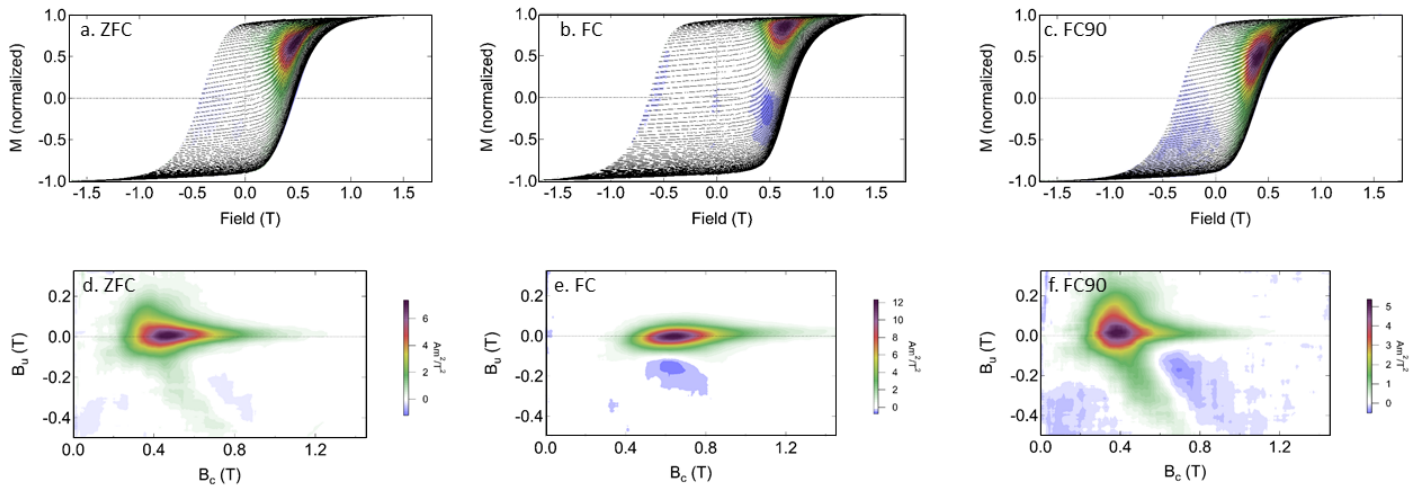


Figure 10. FORC diagrams measured on FF at 100 K and $\phi = 0.14\%$ in (a, d) ZFC, (b, e) FC and (c, f) FC90 configurations.

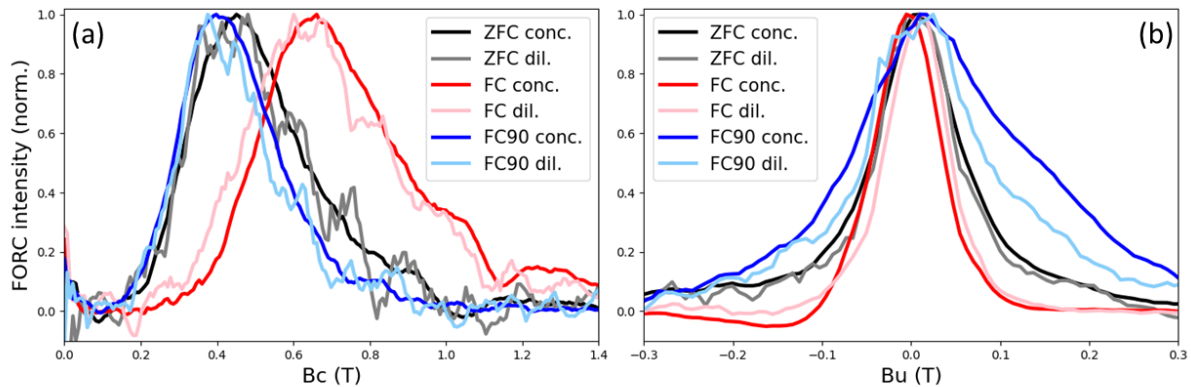


Figure 11. (a) Marginal and (b) vertical profiles from FORC diagrams for diluted and concentrated samples in ZFC, FC and FC90 configurations.

In order to further investigate the macroscopic magnetic properties of the ferrofluid, FORC diagrams were measured on both the concentrated sample ($\phi = 0.14\%$, showing particle assemblies and isolated particles) and the dilute sample ($\phi = 0.014\%$, showing isolated particles).

FORC diagrams, popularized by the field of rock magnetism^{41,42} have become a standard tool to determine the magnetic mineralogy and domain state of natural samples used for environmental

magnetism and paleomagnetism. They contain useful information on the distributions of magnetic properties and magnetization processes. In first approximation, the FORC distribution along the horizontal axis (marginal FORC distribution) can be interpreted as the distribution of the coercive field of the system, and the FORC distribution along the vertical axis as the distribution of the interaction fields of particles.^{41,43}

Three FORC diagrams were measured for each sample: a zero-field cooled diagram (ZFC measurement), a field-cooled diagram (FC measurement), and finally a diagram for which the applied field is perpendicular to the field applied during FC cooling (FC90 measurement).

ZFC FORC diagrams. The FORCs (Figure 10a) have a square shape, with a very large M_r/M_s ratio, which is characteristic of the effect of cubic anisotropy.⁶⁴ The ZFC FORC diagram for $\phi = 0.14$ % forms a tear-drop shape typical of single domain particles⁶⁵ (Fig. 10a, d). This is a clear evidence that despite a complex multi-core structure, the presently investigated CoFe_2O_4 nanoflowers exhibit a magnetic single domain behaviour, which we attribute to the average diameter of 23.5 nm (determined from TEM, below the critical diameter calculated for spherical CoFe_2O_4 particles as $D_c = 40.7$ nm)⁴⁹ and the small mosaicity between crystallites determined from HRTEM. The ZFC FORC diagram for $\phi = 0.014$ % (Fig. S4) has a similar shape to that of the concentrated sample, and also similar marginal / vertical profiles (Fig. 11a, b). In other words, the particle concentration does not impact significantly the distribution of collective magnetic properties under ZFC. It implies that, despite the differences in particle organization observed in cryo-TEM between both samples, magnetic properties under ZFC conditions are dominated by the intrinsic magnetic properties of the nanoparticles (magnetic anisotropy) rather than by their nanoscale organization which is driven by magnetic dipole interactions.

Indeed, comparing anisotropy field $B_k = 2 K_{\text{eff}} / M_s$ with dipolar field $B_{\text{dip}} = 4 \mu_0 M_s V_{\text{mag}} / \pi d^3$ where saturation magnetization $M_s = 264 \text{ kA/m}$ magnetic volume $V_{\text{mag}} = 7194 \text{ nm}^3$ and anisotropy $K_{\text{eff}} = 250 \text{ kJ/m}^3$ for a nanoparticle of diameter $d = 25 \text{ nm}$, we obtain $B_k \sim 10 B_{\text{dip}}$. Hence, dipolar interaction energy is expected to be smaller than anisotropy energy.

Influence of field-cooling on FORC diagrams.

For $\phi = 0.14 \%$, the shape of the FORC contours measured in the FC configuration is more elliptical than in ZFC, with little spread on the vertical axis (Fig. 10b, e). The coercivity distribution is displaced to higher values compared to the ZFC measurement.

This could be related to the difference in particle organization between FC and ZFC observed in cryo-TEM. In the ZFC measurement, MNPs are dispersed in small chains or isolated, and the field necessary to align the moments in the direction of the applied field is directly linked to the dipolar interactions felt by the particles. In the FC measurement, the applied field before cooling leads to the formation of long linear chains of particles. We estimate that these chains may actually be much longer than those observed in cryo-TEM (500 nm-1 μm long), for which we used an applied magnetic field of $\mu_0 H = 20 \text{ mT}$, much smaller than the field applied before cooling in the FORC FC measurement ($\mu_0 H = 1.8 \text{ T}$).

For $\phi = 0.014 \%$, the FC marginal profile (Fig. 11a) shows a coercivity distribution centered at a higher value than for ZFC. This trend is similar to that of the $\phi = 0.14 \%$ case. However, the FC marginal profile for $\phi = 0.014 \%$ is centered at a slightly lower field value than for FC $\phi = 0.14 \%$: this could be an evidence of a less efficient chaining in an applied field, since at such a low concentration, nanoparticles are further apart and less able to form chains.

For $\phi = 0.14 \%$, the FC90 FORC diagram has a tear-drop shape similar to that of the ZFC, but it is more extended along the vertical axis and less along the horizontal axis (Fig. 10c, f), and an additional lobe extending from the main peak in the negative B_u region is visible. These observations are more clearly visible on the marginal profile (Fig. 11a), which shows that switching fields are distributed at higher values and over a larger range in the FC measurement (measuring field along the chain axis) than in the FC90 measurement (measuring field perpendicular to the chain axis). The vertical distribution (Fig. 11b) shows a larger spread of the FORC distribution in the FC90 measurement compare to the FC measurement.

This fingerprint interpretation of the FORC diagrams allows concluding two points. First, the shift in coercivity distribution between ZFC and FC configurations seems to be dependent on particle concentration and thus, on the interaction regime. Second, for the strong interacting case ($\phi = 0.14 \%$), the measured differences between ZFC / FC / FC90 measurements are remarkably different from the ones measured in a FF of 40 nm maghemite particles forming also self-assemblies in ZFC⁶⁶, which might be related to the type of magnetic anisotropy involved (uniaxial for maghemite versus cubic for CoFe_2O_4). In the following, we aim to provide a more quantitative insight into the FORC diagrams using FORC simulations, in particular to understand the relative strength of dipolar interactions with respect to magnetic anisotropy.

Simulations of FORC diagrams.

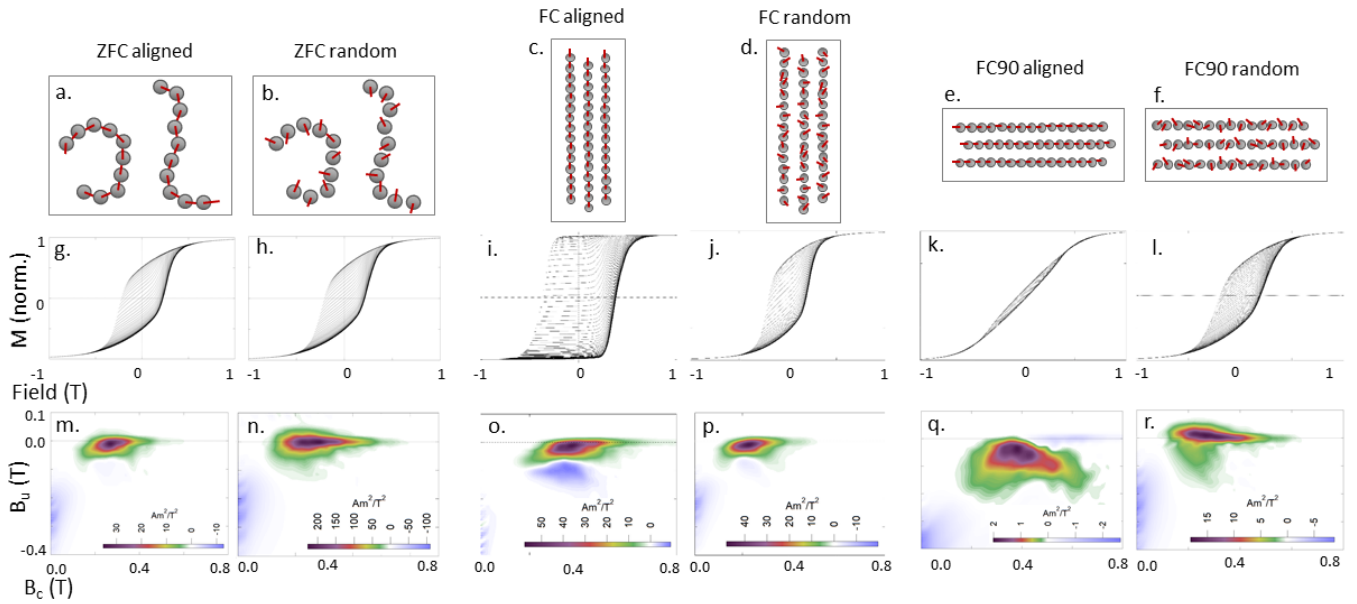


Figure 12. (top) Example of particle configuration used in the FORCulator simulations with the uniaxial anisotropy easy axis represented as a red bar. (middle) Resulting calculated FORCs and (bottom) FORC diagrams. The easy axis of each particle is either aligned with the direction of the chain (labeled aligned) or randomly oriented (labeled random). The different experimental configurations are ZFC with aligned easy axis (a, g, m), ZFC with random easy axis (b, h, n), FC with aligned easy axis (c, i, o), FC with random easy axis (d, j, p), FC90 with aligned easy axis (e, k, q) and FC90 with random easy axis (f, l, r).

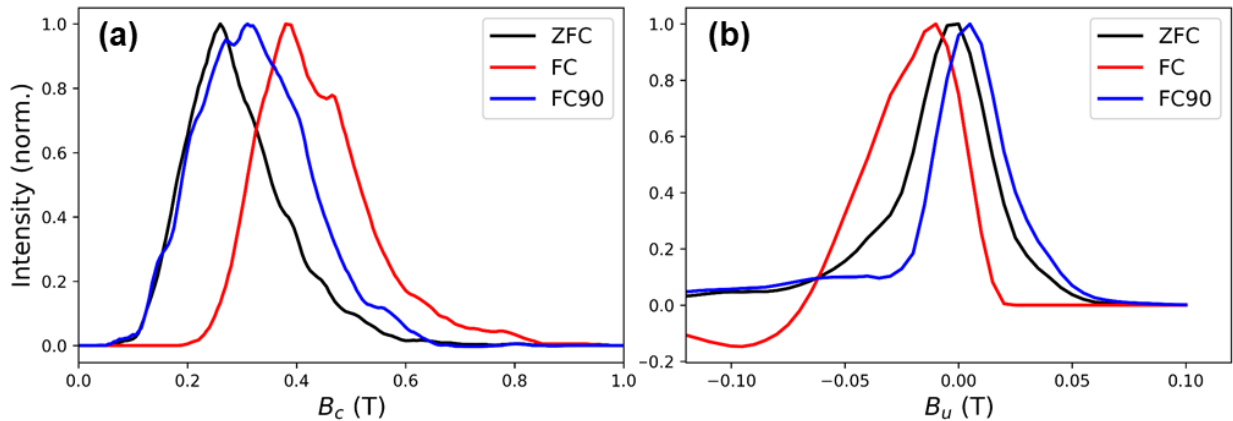


Figure 13. (a) Marginal and (b) vertical profiles extracted from FORC diagrams simulated with FORCulator in configurations ZFC with random orientation of easy axis, FC with easy axis aligned with the chains and FC90 with random orientation of easy axis.

In order to gain a better understanding of the experimental FORC diagrams, several configurations of nanoparticles with uniaxial anisotropy organized in chains were used as models for simulations of FORC diagrams. These models were constrained by our cryo-TEM observations (see Methods), where chains were found to be the most probable type of self-assembly. Cubic anisotropy was also investigated but the current features of the modelling software do not provide the flexibility to modify initial parameters and to model systems that are very different from magnetite, such as the present samples. As a consequence, the FORC diagrams simulated with cubic anisotropy were in disagreement with the experimental ones. The simulations discussed below were therefore performed by considering uniaxial anisotropy for the nanoparticles.

Using the FORCulator software⁴⁷, the ZFC FORC diagram was calculated with particle anisotropy easy axis either aligned with the axis of the chain (Fig. 12a, g, m) or randomly oriented for each particle (Fig. 12b, h, n). The tear-drop shape and main features are in better agreement with the experimental data in the case of the random easy axis model. In other words, collective magnetic properties cannot be reproduced with head-to-tail magnetic moments all parallel to the chain axis, which is consistent with the electron holography observations. They are better reproduced when disorder in the relative orientation of easy axis is accounted for. Our results show that anisotropy dominates magnetic dipole interactions in ZFC conditions. However, the main peak of the ZFC diagram is shifted to lower coercivities with respect to experiment (Fig. 13a). This might be due to the simulation operating at a higher temperature than the experiments (300 K vs 100 K) and it is also observed on the subsequent simulated diagrams.

For the FC configuration, setting all anisotropy easy axis in the direction of the chain provides a FC FORC diagram for which the tear-drop shape is no longer observed (Fig. 12c, i, o), similarly

to the measured FC FORC diagram: the vertical spread on the left side of the FORC peak is reduced and a tail extending to high coercive fields remains (Fig. 12o). Compared to the ZFC measurements, we observed an increase of coercivity distributions, similar to our experimental results. This tail at high coercivity fields is no longer present for the FC FORC diagram simulated with randomly distributed easy axis, nor is the tear-drop shape (Fig. 12d, j, p).

In addition, the distance between nanoparticles was increased to explore the effect of magnetic dipolar interactions on the FORC diagrams. For a distance of 40 nm, interactions (visible in the B_u distribution) become negligible and only the orientation of the easy axis plays a role in the collective magnetic properties. In Fig. S5 the maximum of the marginal distribution is plotted as a function of the distance between nanoparticles. For all distances, the FC aligned configuration shows a larger coercivity than the FC with random axis, the ZFC with aligned and random axis configurations. This is due to the easy axis aligned with the applied field. However, when the distance between the nanoparticles is reduced, the coercivity for the FC aligned configuration increases due to the magnetic dipolar coupling in the chains. We therefore conclude that our experimental measurements show two effects: FC configurations are shifted to higher coercive fields with respect to ZFC for both concentrated and dilute samples due to the alignment of easy axis along the applied field, and the FORC diagram of the concentrated sample is shifted to higher coercive fields with respect to the dilute one, due to the additional magnetic dipolar coupling within the chains.

In FC conditions, collective magnetic properties can therefore be explained by an effective uniaxial anisotropy, which may be related to the structuration in linear chains that are parallel to the measuring field.

Finally, the FC90 FORC diagram modelled with randomly oriented anisotropy easy axis (Fig. 12f, l, r) is in better agreement with experiment than for easy axis oriented in the chain direction (Fig. 12e, k, q): the lobe extending in the lower half of the experimental FC90 FORC diagram as well as the tail along the horizontal axis at high field are present on the randomly oriented anisotropy easy axis FORC diagram, but not on the easy axis oriented in the chain direction. A tentative explanation could be the effect of cubic magnetocrystalline anisotropy of cobalt ferrite: for a given particle one anisotropy easy axis is aligned with the field, but there are two other easy axes available for the magnetic moment to orient itself, both perpendicular to the axis of the chain. This would explain the decrease in coercivity of the entire chain seen in the experimental FC90 data with respect to the one measured in FC.

We note that while marginal distributions for the FC and ZFC configurations are fairly consistent with experimental distributions, this is not the case for the FC90 distribution (Fig. 13a). The agreement is also quite poor between the modelled and measured vertical profiles (Fig. 13b). Nevertheless, these simulations are useful as a first-order qualitative interpretation of the main patterns of FORC diagrams and their evolution under an applied magnetic field.

Finally, it is presently not possible to conclude on the type of effective anisotropy (whether it is uniaxial or cubic) from our FORC simulations, since the FORCulator software results show that differences are reduced when interactions are present⁶⁷. Our experimental results in the FC90 configuration suggest cubic anisotropy as one possibility, and we have attempted to account for it through the introduction of disorder in the easy axes. However, a more refined description of effective anisotropy combined with magnetic dipolar interactions is needed in FORC simulations to confirm the sensitivity of this approach to the type of anisotropy.

CONCLUSION

We investigated a FF composed of cobalt ferrite nanoflowers with various experimental techniques in order to probe structural and magnetic properties from the nanoscale organization to the macroscopic collective magnetic properties. The main results are the following.

First, individual MNPs have a rough and large surface-to-volume ratio, which reduces saturation magnetization compared to bulk cobalt ferrite. The flower-shaped particles are composed of crystallites interconnected by crystalline distortions at the interface. A low stoichiometry of cobalt and a large surface area result in an anisotropy constant that is larger than that of the bulk material ($K = 200 \text{ kJ/m}^3$). Moreover, the nanoflowers were found to be magnetic single-domain.

Second, when studying collective properties, cryo-TEM observations show that the dilute sample contains isolated nanoparticles while the concentrated one has a wide variety of assemblies, with a majority of small chains. However, both samples exhibit similar magnetic properties in ZFC FORC measurements, because the anisotropy energy greatly exceeds the magnetic dipolar energy, an observation which is also consistent with electron holography results. Simulated ZFC FORC diagrams are in fairly good agreement with the experimental ones.

Third, when a magnetic field is applied to the FF, nanoparticles in the concentrated sample form long micrometric chains, as evidenced by cryo-TEM and SAXS measurements, while the dilute sample does not show this chaining effect. For both volume fraction, FC FORC diagrams are shifted to higher coercive fields compared to ZFC diagrams, an effect mostly due to the alignment of the anisotropy easy axis with the applied field. This shift is stronger for the concentrated sample

as the chains contribute to the increase of coercivity through enhanced magnetic dipole interactions.

Our results can help constraining future simulations that involve interacting self-assembled MNPs, as well as providing new insights on the properties of similar FFs under static external magnetic field. Future work can focus on the dynamics of chain formation and the influence of alternative fields on these chains. In addition, as the anisotropy energy greatly exceeds the magnetic dipolar energy in this study, similar measurements would be of interest on a material with reduced anisotropy, such as magnetite.

ASSOCIATED CONTENT

Table S1: Mean diameters obtained from different techniques (TEM, XRD, SAXS and Langevin fit of magnetization curve).

Figure S1. Slice from tomography measurements showing the organization of the nanoflowers in petals around a core with pores and empty spaces between petals. (TIF)

Figure S2. SAXS pattern (orange) for diluted sample ($\phi = 0.014\%$) and SAXS fitting (blue) with monodisperse sphere model of diameter (a) 22 nm, (b) 26 nm and (c) 30 nm. (TIF)

Figure S3. All assemblies observed in electron holography. (TIF)

Figure S4. FORC diagrams measured on the FF at 100 K and $\phi = 0.014\%$ in ZFC, FC and FC90 configurations. (TIF)

Figure S5. Maximum of marginal distribution of simulated FORC diagrams in ZFC and FC configurations, with easy axis aligned with the chain or randomly oriented, for different distance between nanoparticles. (TIF)

AUTHOR INFORMATION

Corresponding Authors

*amelie.juhin@sorbonne-universite.fr

Author Contributions

The manuscript was written through contributions of all authors. All authors have given approval to the final version of the manuscript.

Funding Sources

ACKNOWLEDGMENT

Authors acknowledge financial support from the French ANR under grant agreement 17-410 CE30-0010-01. The authors acknowledge financial support from the CNRS-CEA “METSAs” French network (FR CNRS 3507) on the CEMES platform.

REFERENCES

- (1) Dutz, S.; Hergt, R. Magnetic Particle Hyperthermia—a Promising Tumour Therapy? *Nanotechnology* **2014**, *25* (45), 452001. <https://doi.org/10.1088/0957-4484/25/45/452001>.
- (2) Israel, L. L.; Galstyan, A.; Holler, E.; Ljubimova, J. Y. Magnetic Iron Oxide Nanoparticles for Imaging, Targeting and Treatment of Primary and Metastatic Tumors of the Brain. *J. Controlled Release* **2020**, *320*, 45–62. <https://doi.org/10.1016/j.jconrel.2020.01.009>.
- (3) Xiao, Y.; Du, J. Superparamagnetic Nanoparticles for Biomedical Applications. *J. Mater. Chem. B* **2020**, *8* (3), 354–367. <https://doi.org/10.1039/C9TB01955C>.
- (4) Torres-Díaz, I.; Rinaldi, C. Recent Progress in Ferrofluids Research: Novel Applications of Magnetically Controllable and Tunable Fluids. *Soft Matter* **2014**, *10* (43), 8584–8602. <https://doi.org/10.1039/C4SM01308E>.

- (5) Kodama, S. Dynamic Ferrofluid Sculpture: Organic Shape-Changing Art Forms. *Commun. ACM* **2008**, *51* (6), 79–81. <https://doi.org/10.1145/1349026.1349042>.
- (6) Peddis, D.; Yaacoub, N.; Ferretti, M.; Martinelli, A.; Piccaluga, G.; Musinu, A.; Cannas, C.; Navarra, G.; Greneche, J. M.; Fiorani, D. Cationic Distribution and Spin Canting in CoFe_2O_4 Nanoparticles. *J. Phys. Condens. Matter* **2011**, *23* (42), 426004. <https://doi.org/10.1088/0953-8984/23/42/426004>.
- (7) Martinez-Boubeta, C.; Simeonidis, K.; Makridis, A.; Angelakeris, M.; Iglesias, O.; Guardia, P.; Cabot, A.; Yedra, L.; Estradé, S.; Peiró, F.; Saghi, Z.; Midgley, P. A.; Conde-Leborán, I.; Serantes, D.; Baldomir, D. Learning from Nature to Improve the Heat Generation of Iron-Oxide Nanoparticles for Magnetic Hyperthermia Applications. *Sci. Rep.* **2013**, *3* (1), 1652. <https://doi.org/10.1038/srep01652>.
- (8) Di, Z.; Chen, X.; Pu, S.; Hu, X.; Xia, Y. Magnetic-Field-Induced Birefringence and Particle Agglomeration in Magnetic Fluids. *Appl. Phys. Lett.* **2006**, *89* (21), 211106. <https://doi.org/10.1063/1.2392824>.
- (9) Kantorovich, S.; Ivanov, A. O.; Rovigatti, L.; Tavares, J. M.; Sciortino, F. Nonmonotonic Magnetic Susceptibility of Dipolar Hard-Spheres at Low Temperature and Density. *Phys. Rev. Lett.* **2013**, *110* (14), 148306. <https://doi.org/10.1103/PhysRevLett.110.148306>.
- (10) Gennes, P. G.; Pincus, P. A. Pair Correlations in a Ferromagnetic Colloid. *Phys. Kondens. Mater.* **1970**, *11* (3), 189–198. <https://doi.org/10.1007/BF02422637>.
- (11) Kantorovich, S. S.; Ivanov, A. O.; Rovigatti, L.; Tavares, J. M.; Sciortino, F. Temperature-Induced Structural Transitions in Self-Assembling Magnetic Nanocolloids. *Phys. Chem. Chem. Phys.* **2015**, *17* (25), 16601–16608. <https://doi.org/10.1039/C5CP01558H>.
- (12) Elfimova, E. A.; Ivanov, A. O.; Camp, P. J. Static Magnetization of Immobilized, Weakly Interacting, Superparamagnetic Nanoparticles. *Nanoscale* **2019**, *11* (45), 21834–21846. <https://doi.org/10.1039/C9NR07425B>.
- (13) Usov, N. A.; Barandiarán, J. M. Magnetic Nanoparticles with Combined Anisotropy. *J. Appl. Phys.* **2012**, *112* (5), 053915. <https://doi.org/10.1063/1.4749799>.
- (14) Klokkenburg, M.; Erné, B. H.; Mendeleev, V.; Ivanov, A. O. Magnetization Behavior of Ferrofluids with Cryogenically Imaged Dipolar Chains. *J. Phys. Condens. Matter* **2008**, *20* (20), 204113. <https://doi.org/10.1088/0953-8984/20/20/204113>.
- (15) Ivanov, A. O.; Kantorovich, S. S.; Zverev, V. S.; Elfimova, E. A.; Lebedev, A. V.; Pshenichnikov, A. F. Temperature-Dependent Dynamic Correlations in Suspensions of Magnetic Nanoparticles in a Broad Range of Concentrations: A Combined Experimental and Theoretical Study. *Phys. Chem. Chem. Phys.* **2016**, *18* (27), 18342–18352. <https://doi.org/10.1039/c6cp02793h>.
- (16) Holm, C.; Ivanov, A.; Kantorovich, S.; Pyanzina, E.; Reznikov, E. Equilibrium Properties of a Bidisperse Ferrofluid with Chain Aggregates: Theory and Computer Simulations. *J. Phys. Condens. Matter* **2006**, *18* (38), S2737–S2756. <https://doi.org/10.1088/0953-8984/18/38/S14>.
- (17) Weis, J. J.; Levesque, D. Chain Formation in Low Density Dipolar Hard Spheres: A Monte Carlo Study. *Phys. Rev. Lett.* **1993**, *71* (17), 2729–2732. <https://doi.org/10.1103/PhysRevLett.71.2729>.
- (18) Camp, P. J.; Ivanov, A. O. Modified Mean-Field Theory of One-Dimensional Spin Models with Anisotropy and Long-Range Dipolar Interactions. *Ukr. J. Phys.* **2020**, *65* (8), 691–700. <https://doi.org/10.15407/ujpe65.8.691>.

- (19) Klokkenburg, M.; Vonk, C.; Claesson, E. M.; Meeldijk, J. D.; Ern , B. H.; Philipse, A. P. Direct Imaging of Zero-Field Dipolar Structures in Colloidal Dispersions of Synthetic Magnetite. *J. Am. Chem. Soc.* **2004**, *126* (51), 16706–16707. <https://doi.org/10.1021/ja0456252>.
- (20) Klokkenburg, M.; Ern , B. H.; Meeldijk, J. D.; Wiedenmann, A.; Petukhov, A. V.; Dullens, R. P. A.; Philipse, A. P. In Situ Imaging of Field-Induced Hexagonal Columns in Magnetite Ferrofluids. *Phys. Rev. Lett.* **2006**, *97* (18), 185702. <https://doi.org/10.1103/PhysRevLett.97.185702>.
- (21) Rosenfeldt, S.; Riese, C. N.; Mickoleit, F.; Sch ler, D.; Schenk, A. S. Probing the Nanostructure and Arrangement of Bacterial Magnetosomes by Small-Angle X-Ray Scattering. *Appl. Environ. Microbiol.* **2019**, *85* (24), e01513-19. <https://doi.org/10.1128/AEM.01513-19>.
- (22) Bender, P.; Honecker, D.; Fern ndez Barqu n, L. Supraferromagnetic Correlations in Clusters of Magnetic Nanoflowers. *Appl. Phys. Lett.* **2019**, *115* (13), 132406. <https://doi.org/10.1063/1.5121234>.
- (23) Dunin-Borkowski, R. E.; Kasama, T.; Wei, A.; Tripp, S. L.; H tch, M. J.; Snoeck, E.; Harrison, R. J.; Putnis, A. Off-Axis Electron Holography of Magnetic Nanowires and Chains, Rings, and Planar Arrays of Magnetic Nanoparticles: Electron Holography of Magnetic Nanostructures. *Microsc. Res. Tech.* **2004**, *64* (5–6), 390–402. <https://doi.org/10.1002/jemt.20098>.
- (24) Rastei, M. V.; Pierron-Bohnes, V.; Toulemon, D.; Bouillet, C.; K kay, A.; Hertel, R.; Tetsi, E.; Begin-Colin, S.; Pichon, B. P. Defect-Driven Magnetization Configuration of Isolated Linear Assemblies of Iron Oxide Nanoparticles. *Adv. Funct. Mater.* **2019**, *29* (45), 1903927. <https://doi.org/10.1002/adfm.201903927>.
- (25) Dunin-Borkowski, R. E.; McCartney, M. R.; Frankel, R. B.; Bazylinski, D. A.; P sfai, M.; Buseck, P. R. Magnetic Microstructure of Magnetotactic Bacteria by Electron Holography. *Science* **1998**, *282* (5395), 1868–1870. <https://doi.org/10.1126/science.282.5395.1868>.
- (26) Snoeck, E.; Gatel, C.; Lacroix, L. M.; Blon, T.; Lachaize, S.; Carrey, J.; Respaud, M.; Chaudret, B. Magnetic Configurations of 30 Nm Iron Nanocubes Studied by Electron Holography. *Nano Lett.* **2008**, *8* (12), 4293–4298. <https://doi.org/10.1021/nl801998x>.
- (27) Var n, M.; Beleggia, M.; Kasama, T.; Harrison, R. J.; Dunin-Borkowski, R. E.; Punties, V. F.; Frandsen, C. Dipolar Magnetism in Ordered and Disordered Low-Dimensional Nanoparticle Assemblies. *Sci. Rep.* **2013**, *3* (1), 1234. <https://doi.org/10.1038/srep01234>.
- (28) Blondeau, M.; Guyodo, Y.; Guyot, F.; Gatel, C.; Menguy, N.; Chebbi, I.; Haye, B.; Durand-Dubief, M.; Alphantery, E.; Brayner, R.; Coradin, T. Magnetic-Field Induced Rotation of Magnetosome Chains in Silicified Magnetotactic Bacteria. *Sci. Rep.* **2018**, *8* (1), 7699. <https://doi.org/10.1038/s41598-018-25972-x>.
- (29) Andersen, I. M.; Wolf, D.; Rodriguez, L. A.; Lubk, A.; Oliveros, D.; Bran, C.; Niermann, T.; R bller, U. K.; Vazquez, M.; Gatel, C.; Snoeck, E. Field Tunable Three-Dimensional Magnetic Nanotextures in Cobalt-Nickel Nanowires. *Phys. Rev. Res.* **2021**, *3* (3), 033085. <https://doi.org/10.1103/PhysRevResearch.3.033085>.
- (30) Klokkenburg, M.; Ern , B. H.; Wiedenmann, A.; Petukhov, A. V.; Philipse, A. P. Dipolar Structures in Magnetite Ferrofluids Studied with Small-Angle Neutron Scattering with and without Applied Magnetic Field. *Phys. Rev. E* **2007**, *75* (5), 051408. <https://doi.org/10.1103/PhysRevE.75.051408>.

- (31) Salazar-Alvarez, G.; Qin, J.; Šepelák, V.; Bergmann, I.; Vasilakaki, M.; Trohidou, K. N.; Ardisson, J. D.; Macedo, W. A. A.; Mikhaylova, M.; Muhammed, M.; Baró, M. D.; Nogués, J. Cubic versus Spherical Magnetic Nanoparticles: The Role of Surface Anisotropy. *J. Am. Chem. Soc.* **2008**, *130* (40), 13234–13239. <https://doi.org/10.1021/ja0768744>.
- (32) Butter, K.; Bomans, P. H. H.; Frederik, P. M.; Vroege, G. J.; Philipse, A. P. Direct Observation of Dipolar Chains in Iron Ferrofluids by Cryogenic Electron Microscopy. *Nat. Mater.* **2003**, *2* (2), 88–91. <https://doi.org/10.1038/nmat811>.
- (33) Peddis, D.; Cannas, C.; Musinu, A.; Ardu, A.; Orrù, F.; Fiorani, D.; Laureti, S.; Rinaldi, D.; Muscas, G.; Concas, G.; Piccaluga, G. Beyond the Effect of Particle Size: Influence of CoFe₂O₄ Nanoparticle Arrangements on Magnetic Properties. *Chem. Mater.* **2013**, *25* (10), 2005–2013. <https://doi.org/10.1021/cm303352r>.
- (34) Gavilán, H.; Simeonidis, K.; Myrovali, E.; Mazarío, E.; Chubykalo-Fesenko, O.; Chantrell, R.; Balcells, Ll.; Angelakeris, M.; Morales, M. P.; Serantes, D. How Size, Shape and Assembly of Magnetic Nanoparticles Give Rise to Different Hyperthermia Scenarios. *Nanoscale* **2021**, *13* (37), 15631–15646. <https://doi.org/10.1039/D1NR03484G>.
- (35) Bender, P.; Fock, J.; Frandsen, C.; Hansen, M. F.; Balceris, C.; Ludwig, F.; Posth, O.; Wetterskog, E.; Bogart, L. K.; Southern, P.; Szczerba, W.; Zeng, L.; Witte, K.; Grüttner, C.; Westphal, F.; Honecker, D.; González-Alonso, D.; Fernández Barquín, L.; Johansson, C. Relating Magnetic Properties and High Hyperthermia Performance of Iron Oxide Nanoflowers. *J. Phys. Chem. C* **2018**, *122* (5), 3068–3077. <https://doi.org/10.1021/acs.jpcc.7b11255>.
- (36) Neumann, S.; Kuger, L.; Arlt, C.-R.; Franzreb, M.; Rafaja, D. Influence of the Hierarchical Architecture of Multi-Core Iron Oxide Nanoflowers on Their Magnetic Properties. *Sci. Rep.* **2023**, *13* (1), 1–14. <https://doi.org/10.1038/s41598-023-31294-4>.
- (37) Caruntu, D.; Caruntu, G.; Chen, Y.; O'Connor, C. J.; Goloverda, G.; Kolesnichenko, V. L. Synthesis of Variable-Sized Nanocrystals of Fe₃O₄ with High Surface Reactivity. *Chem. Mater.* **2004**, *16* (25), 5527–5534. <https://doi.org/10.1021/cm0487977>.
- (38) Ammar, S.; Helfen, A.; Jouini, N.; Fiévet, F.; Rosenman, I.; Villain, F.; Molinié, P.; Danot, M. Magnetic Properties of Ultrafine Cobalt Ferrite Particles Synthesized by Hydrolysis in a Polyol Medium. *J. Mater. Chem.* **2001**, *11* (1), 186–192. <https://doi.org/10.1039/b003193n>.
- (39) Lefebure, S.; Dubois, E.; Cabuil, V.; Neveu, S.; Massart, R. Monodisperse Magnetic Nanoparticles: Preparation and Dispersion in Water and Oils. *J. Mater. Res.* **1998**, *13* (10), 2975–2981. <https://doi.org/10.1557/JMR.1998.0407>.
- (40) Holzwarth, U.; Gibson, N. The Scherrer Equation versus the “Debye-Scherrer Equation.” *Nat. Nanotechnol.* **2011**, *6* (9), 534–534. <https://doi.org/10.1038/nnano.2011.145>.
- (41) Roberts, A. P.; Pike, C. R.; Verosub, K. L. First-Order Reversal Curve Diagrams: A New Tool for Characterizing the Magnetic Properties of Natural Samples. *J. Geophys. Res. Solid Earth* **2000**, *105* (B12), 28461–28475. <https://doi.org/10.1029/2000JB900326>.
- (42) Pike, C. R.; Roberts, A. P.; Verosub, K. L. Characterizing Interactions in Fine Magnetic Particle Systems Using First Order Reversal Curves. *J. Appl. Phys.* **1999**, *85* (9), 6660–6667. <https://doi.org/10.1063/1.370176>.
- (43) Egli, R. Theoretical Aspects of Dipolar Interactions and Their Appearance in First-Order Reversal Curves of Thermally Activated Single-Domain Particles. *J. Geophys. Res. Solid Earth* **2006**, *111* (B12). <https://doi.org/10.1029/2006JB004567>.

- (44) Winklhofer, M.; Zimanyi, G. T. Extracting the Intrinsic Switching Field Distribution in Perpendicular Media: A Comparative Analysis. *J. Appl. Phys.* **2006**, *99* (8). <https://doi.org/10.1063/1.2176598>.
- (45) Harrison, R. J.; Feinberg, J. M. FORCinel: An Improved Algorithm for Calculating First-Order Reversal Curve Distributions Using Locally Weighted Regression Smoothing: FORCINEL ALGORITHM. *Geochem. Geophys. Geosystems* **2008**, *9* (5), n/a-n/a. <https://doi.org/10.1029/2008GC001987>.
- (46) Egli, R. VARIFORC: An Optimized Protocol for Calculating Non-Regular First-Order Reversal Curve (FORC) Diagrams. *Glob. Planet. Change* **2013**, *110*, 302–320. <https://doi.org/10.1016/j.gloplacha.2013.08.003>.
- (47) Harrison, R. J.; Lascu, I. FORCulator: A Micromagnetic Tool for Simulating First-Order Reversal Curve Diagrams. *Geochem. Geophys. Geosystems* **2014**, *15* (12), 4671–4691. <https://doi.org/10.1002/2014GC005582>.
- (48) Daffé, N.; Choueikani, F.; Neveu, S.; Arrio, M.-A.; Juhin, A.; Ohresser, P.; Dupuis, V.; Saintavit, P. Magnetic Anisotropies and Cationic Distribution in CoFe₂O₄ Nanoparticles Prepared by Co-Precipitation Route: Influence of Particle Size and Stoichiometry. *J. Magn. Magn. Mater.* **2018**, *460*, 243–252. <https://doi.org/10.1016/j.jmmm.2018.03.041>.
- (49) Torres, T. E.; Lima, E.; Mayoral, A.; Ibarra, A.; Marquina, C.; Ibarra, M. R.; Goya, G. F. Validity of the Néel-Arrhenius Model for Highly Anisotropic Co_xFe_{3-x}O₄ Nanoparticles. *J. Appl. Phys.* **2015**, *118* (18), 183902. <https://doi.org/10.1063/1.4935146>.
- (50) Lartigue, L.; Hugounenq, P.; Alloyeau, D.; Clarke, S. P.; Lévy, M.; Bacri, J.-C.; Bazzi, R.; Brougham, D. F.; Wilhelm, C.; Gazeau, F. Cooperative Organization in Iron Oxide Multi-Core Nanoparticles Potentiates Their Efficiency as Heating Mediators and MRI Contrast Agents. *ACS Nano* **2012**, *6* (12), 10935–10949. <https://doi.org/10.1021/nn304477s>.
- (51) Bertuit, E.; Menguy, N.; Wilhelm, C.; Rollet, A.-L.; Abou-Hassan, A. Angular Orientation between the Cores of Iron Oxide Nanoclusters Controls Their Magneto–Optical Properties and Magnetic Heating Functions. *Commun. Chem.* **2022**, *5* (1), 1–10. <https://doi.org/10.1038/s42004-022-00787-0>.
- (52) Bertuit, E.; Benassai, E.; Mériguet, G.; Greneche, J.-M.; Baptiste, B.; Neveu, S.; Wilhelm, C.; Abou-Hassan, A. Structure–Property–Function Relationships of Iron Oxide Multicore Nanoflowers in Magnetic Hyperthermia and Photothermia. *ACS Nano* **2022**, *16* (1), 271–284. <https://doi.org/10.1021/acsnano.1c06212>.
- (53) Hugounenq, P.; Levy, M.; Alloyeau, D.; Lartigue, L.; Dubois, E.; Cabuil, V.; Ricolleau, C.; Roux, S.; Wilhelm, C.; Gazeau, F.; Bazzi, R. Iron Oxide Monocrystalline Nanoflowers for Highly Efficient Magnetic Hyperthermia. *J. Phys. Chem. C* **2012**, *116* (29), 15702–15712. <https://doi.org/10.1021/jp3025478>.
- (54) Thomas, G.; Demoisson, F.; Chassagnon, R.; Popova, E.; Millot, N. One-Step Continuous Synthesis of Functionalized Magnetite Nanoflowers. *Nanotechnology* **2016**, *27* (13), 135604. <https://doi.org/10.1088/0957-4484/27/13/135604>.
- (55) Guinier, A.; Fournet, G. Small-Angle Scattering of X-Rays. *Struct. Matter Ser.* Wiley **1955**.
- (56) Glatter, O.; Kratky, O. Small Angle X-Ray Scattering. *Acad. Press* **1982**.
- (57) Gatel, C.; Bonilla, F. J.; Meffre, A.; Snoeck, E.; Warot-Fonrose, B.; Chaudret, B.; Lacroix, L.-M.; Blon, T. Size-Specific Spin Configurations in Single Iron Nanomagnet: From Flower to Exotic Vortices. *Nano Lett.* **2015**, *15* (10), 6952–6957. <https://doi.org/10.1021/acs.nanolett.5b02892>.

- (58) Fu, S.; Yang, R.; Ren, J.; Liu, J.; Zhang, L.; Xu, Z.; Kang, Y.; Xue, P. Catalytically Active CoFe_2O_4 Nanoflowers for Augmented Sonodynamic and Chemodynamic Combination Therapy with Elicitation of Robust Immune Response. *ACS Nano* **2021**, *15* (7), 11953–11969. <https://doi.org/10.1021/acsnano.1c03128>.
- (59) Cullity, B. D.; Graham, C. D. *Introduction to Magnetic Materials*; John Wiley & Sons, 2011.
- (60) Bishop, K. J. M.; Wilmer, C. E.; Soh, S.; Grzybowski, B. A. Nanoscale Forces and Their Uses in Self-Assembly. *Small* **2009**, *5* (14), 1600–1630. <https://doi.org/10.1002/smll.200900358>.
- (61) Sathya, A.; Guardia, P.; Brescia, R.; Silvestri, N.; Pugliese, G.; Nitti, S.; Manna, L.; Pellegrino, T. $\text{CoFe}_3\text{-xO}_4$ Nanocubes for Theranostic Applications: Effect of Cobalt Content and Particle Size. *Chem. Mater.* **2016**, *28* (6), 1769–1780. <https://doi.org/10.1021/acs.chemmater.5b04780>.
- (62) Sharifi Dehsari, H.; Asadi, K. Impact of Stoichiometry and Size on the Magnetic Properties of Cobalt Ferrite Nanoparticles. *J. Phys. Chem. C* **2018**, *122* (51), 29106–29121. <https://doi.org/10.1021/acs.jpcc.8b09276>.
- (63) Stoner, E. C. A Mechanism of Magnetic Hysteresis in Heterogeneous Alloys. 44.
- (64) Valdez-Grijalva, M. A.; Muxworthy, A. R. First-Order Reversal Curve (FORC) Diagrams of Nanomagnets with Cubic Magnetocrystalline Anisotropy: A Numerical Approach. *J. Magn. Magn. Mater.* **2019**, *471*, 359–364. <https://doi.org/10.1016/j.jmmm.2018.09.086>.
- (65) Roberts, A. P.; Heslop, D.; Zhao, X.; Pike, C. R. Understanding Fine Magnetic Particle Systems through Use of First-Order Reversal Curve Diagrams: FORC Diagrams. *Rev. Geophys.* **2014**, *52* (4), 557–602. <https://doi.org/10.1002/2014RG000462>.
- (66) Carvallo, C.; Fondet, A.; Le Fèvre, R.; Taverna, D.; Guyodo, Y.; Chebbi, I.; Dupuis, V.; Lagroix, F.; Khelfallah, M.; Guigner, J.-M.; Guyot, F.; Alphanéry, E.; Juhin, A. Magnetic and Structural Properties of Biogenic Magnetic Nanoparticles along Their Production Process for Use in Magnetic Hyperthermia. *J. Magn. Magn. Mater.* **2023**, *575*, 170726. <https://doi.org/10.1016/j.jmmm.2023.170726>.
- (67) Harrison, R. J.; Zhao, X.; Hu, P.; Sato, T.; Heslop, D.; Muxworthy, A. R.; Oda, H.; Kuppili, V. S. C.; Roberts, A. P. Simulation of Remanent, Transient, and Induced FORC Diagrams for Interacting Particles With Uniaxial, Cubic, and Hexagonal Anisotropy. *J. Geophys. Res. Solid Earth* **2019**, *124* (12), 12404–12429. <https://doi.org/10.1029/2019JB018050>.